FINAL SCIENTIFIC REPORT

Project Title: Distributed Wireless Antenna Sensors for Boiler Condition Monitoring

Reporting Period Start Date: 1/1/2015

Reporting Period End Date: 12/31/2018 (with one-year no-cost extension)

Principal Author(s):

PI: Haiying Huang, Ph.D
Dept. of Mechanical and Aerospace Engineering
University of Texas Arlington, Arlington-TX
Tel: (817) 272-0563
Fax: (817) 272-5010
Email: huang@uta.edu

Co-PI: Ankur Jain, Ph.D.
Dept. of Mechanical and Aerospace Engineering
University of Texas Arlington, Arlington-TX
Tel: (817)-272-9338
Fax: (817)-272-5010
Email: jaina@uta.edu

Co-PI: Jian Luo, Ph.D.
Dept. of Nano Engineering
University of California, San Diego
San Diego, CA
Tel: (858) 246-1203
Fax: (858) 534-9553
Email: jluo@ucsd.edu

Student: Franck Mbanya Tchafa
Dept. of Mechanical and Aerospace Engineering
University of Texas Arlington, Arlington-TX

Student: Jun Yao
Dept. of Electrical Engineering
University of Texas Arlington, Arlington-TX

Student: Jiuyuan Nie
Dept. of Nano Engineering
University of California, San Diego
San Diego, CA

Report Date: March 28, 2019

DOE Award Number: DE- FE0023118

Name and Address of Submitting Organization: University of Texas Arlington
202 E. Border, Suite 216
Box 19145
Arlington, TX, 76019-0145

DISCLAIMER

ABSTRACT

Monitoring the operational conditions of coal-fired boilers is an important task that could bring tremendous benefits, including in-situ process control, real-time health assessment of structural components, improved heat transfer efficiency, reduced downtime, etc. Moreover, in-situ distributed sensing of the boiler conditions would provide large scale in-situ measurement data that will help us gain fundamental understandings of the combustion and heat transfer processes as well as enable the developments of new simulation tools, which could eventually lead to better design and more efficient operation of the boilers. The objectives of this research were to (a) develop wireless passive antenna sensors without electronics; (b) demonstrate multi-modality sensing using a signal antenna sensor; and (c) fabricate the antenna sensor from high-temperature materials. In this project, we have demonstrated that an antenna sensor or sensor array without any electronics can be wirelessly interrogated from a distance. In addition, a low-cost compact wireless sensor interrogator was developed for dynamic interrogation of the passive antenna sensor. We validated that a dual-frequency antenna sensor is capable of simultaneous strain and temperature measurements or temperature and ash accumulation measurements; all parameters are relevant to boiler condition monitoring. By measuring the temperature and ash accumulation height simultaneously, the dielectric constant of the ash as well as its temperature dependency can also be characterized. This capability could lead to potential applications of the antenna sensor for combustion process monitoring based on the ash composition. We also investigated different techniques of fabricating the antenna sensor using high-temperature materials such as alumina substrate and platinum paste and characterized the thermal response of the antenna sensor. A linear relationship between the antenna resonant frequency and the temperature change was validated.

TABLE OF CONTENTS

EXECUTIVE SUMMARY

The goal of this project was to develop fully passive, wireless antenna sensors for distributed condition monitoring of coal-fired boilers at low cost. The project was meant to address the limitation of current sensing technologies in ensuring safe and efficient operations of coal-fired boilers. This project has been focusing on: 1) demonstrating wireless interrogation of antenna sensor and sensor arrays without electronics at the sensor node; 2) validating the antenna sensor's capability for sensing multiple measurands simultaneously; 3) investigating techniques to fabricate antenna sensors from high-temperature materials. This project has led to two PhD dissertations, two journal publications (with one additional journal manuscript under review), and two conference presentations. This project was a collaborative effort involving researchers from two universities with different technical, ethnicity, and racial backgrounds.

Conventional wireless sensors typically need electronic circuits at the sensor node to provide wireless communication capability. Their maximum operating temperature is thus limited by the temperature tolerance of the onboard electronics. In order to provide sensing capabilities at higher temperatures, we investigated wireless interrogation of antenna sensors without any electronics at the sensor node. By connecting the antenna sensor to an ultra-wideband antenna using a microstrip transmission line, we developed techniques to separate the sensing signal from the background clutter. Wireless interrogation of the antenna sensor was demonstrated from a distance of about one meter while the antenna sensor was enclosed inside a furnace and the interrogator was placed outside the furnace. The study also demonstrated that antenna sensors fabricated from commercially available printed circuit board can provide linear temperature measurements up to 270°C. Moreover, an antenna sensor array was realized by designing each antenna sensor to have a different resonant frequency and wireless interrogation of the antenna sensor array without electronics was demonstrated. This development could lead to low-cost deployment of antenna sensors and sensor arrays for various condition monitoring schemes.

Most research works on wireless interrogation of antenna sensors have been carried out using expensive and bulky laboratory instruments (e.g. a vector network analyzer) that also have a slow sampling rate. In this study, we developed a compact, low-cost wireless interrogator based on the principle of Frequency Modulated Continuous Wave (FMCW) radar and demonstrated it for dynamic interrogation of the antenna sensor at a high interrogation speed of 50 Hz. The interrogator produced comparable results as those provided by a laboratory instrument; the normalized discrepancies of two measurements are within 0.002%. To further reduce the size of the wireless interrogator, an FMCW signal source was designed and implemented using surface-mount integrated circuit components; it has a size of a business card, a low power consumption of 160 mW, and provides a sampling rate of 55 Hz. Such an interrogator reduces the size and cost of the sensing system substantially, further extending the functionality of the antenna sensor from static to dynamic measurements (e.g., vibration).

For the safe and efficient operation of coal-burning boilers, we identified three key measurands–temperature, strain, and ash thickness–that must be extracted from the antenna sensor response. By taking advantage of a dual-frequency antenna sensor, we established a procedure to extract two measurement parameters simultaneously from one sensor response. The antenna sensor was characterized under a combination of temperature and strain levels. The temperatures and strains inversely determined from the normalized frequency shifts had a measurement uncertainty of ±0.4ºC and ±17.22 με, respectively. This multi-variant sensing capability enables temperature-compensated strain measurements and thus resolved a long-standing challenge of strain-temperature cross-sensitivity facing many conventional strain sensors. For simultaneous temperature and ash thickness measurements, the measurement uncertainties was determined to be ±0.58°C for temperature and ±58.05 μm for ash

thickness measurements. Simultaneous measurements of temperature and ash thickness also enabled determining the dielectric constant of the ash at different temperatures. As a result, the temperature dependency of the ash dielectric constant can be characterized. Ash dielectric constant is highly dependent of coal composition and combustion condition. Potentially, this technique can be extended for monitoring the combustion process based on the measured ash dielectric constant and its temperature dependency.

By removing electronics from the wireless sensor nodes, the maximum operating temperature of the antenna sensor is no longer limited by the electronics but the dielectric and conductive materials, some of which can sustain extremely-high temperatures. In this study, we investigated implementing the antenna sensors on high-temperature materials such as alumina and platinum. Platinum paste was tape casted on alumina substrates based on the designed patterns, followed by drying and firing. To control the dimension of the antenna pattern, laser machining was employed to trim the pasted pattern. In addition, sensor implementation using commercial metalized alumina substrates was also explored. The thermal response of the antenna sensor fabricated from these high-temperature materials was characterized. For the antenna sensor fabricated using alumina substrate and platinum paste, the measured temperature sensitivity of the antenna resonant frequency is -71.71 ppm/^{o}C with an excellent linearity. The thermal response of the dielectric constant (TCD_k) was found to be 127.5 ppm/^{o}C for the alumina substrate. For the commercial metalized alumina susbtrate, the temperature sensitivity of the antenna resonant frequency was measured to be -63.59 ppm/^{o}C. This corresponds to a TCDk of 114 ppm/ ^{o}C for the commercial alumina substrate. The temperature measurement error was estimated to be $\pm$0.3^{o}C.

In summary, this project studied the realization of antenna sensor and sensor arrays for measuring parameters that are relevant to condition monitoring of coal-fired boilers. A key technology developed was the capability of providing wireless sensing without any electronics at the sensor node. This development eliminates the temperature limit imposed by electronics, substantially increasing the operating temperature range of the antenna sensors. Secondly, dual-frequency antenna sensors were characterized for measuring two different yet interdependent measurands simultaneously. The capabilities of measuring strain and temperature as well as temperature and ash thickness have been validated. As a by-product, the antenna sensor is also capable of measuring the dielectric constant of ash and its temperature dependency. Thirdly, fabricating the antenna sensors from high-temperature materials (e.g., aluminum susbtrate and platinum) was explored. Thermal testing of the fabricated antenna sensors produced linear responses with temperature changes. Overall, this research confirmed the original hypothesis that wireless passive antenna sensors have the potential for condition monitoring at temperature as high as 1000^{o}C.

LIST OF FIGURES

ACCOMPLISHED TASKS

1. Demonstrate wireless interrogation of passive antenna sensors and sensor arrays

Publications:

J. Yao, F. Tchafa, H. Huang, "Far-field interrogation of patch antenna for temperature sensing without electronics", *IEEE Sens. J.,* vol. 16, no. 19, pp. 7053–7060, 2016.
F. Tchafa, J. Yao, H. Huang, "Wireless interrogation of a high-temperature antenna sensor without electronics", presented at the ASME International Mechanical Engineering Congress and Exposition, November 11-17, 2016, Phoenix, Arizona.

1.1. Wireless interrogation of antenna sensor for temperature sensing up to 270°C

The maximum operating temperature of sensors containing onboard electronics are limited by the electronics. In order to provide sensing capabilities at temperatures beyond this temperature limit, we investigated wireless interrogation of antenna sensors without any electronics at the sensor node.

Experimental methods: Figure 1 presents the sensor node that we developed and tested for demonstrating such capabilities. The sensor node was fabricated from commercial high-temperature substrate (Rogers 3210). It is entirely passive and consists of a microstrip patch antenna as the temperature sensing element and an ultrawideband (UWB) transmitting and receiving (Tx/Rx) antenna for wireless communication. A microstrip transmission line connecting the UWB Tx/Rx antenna and the antenna sensor delays the sensing signal and thus separates it from the background clutter. Temperature change is measured from the frequency shift of the antenna sensor because the dielectric constant of the substrate is temperature dependent. In addition, the radiation patch dimensions also change with temperature because of thermal expansion. The principle of operation of the wireless sensing scheme, and the design of the antenna sensor package are discussed in details in the above publications. Furthermore, a digital signal processing algorithm that extracts the antenna resonant frequency from the wirelessly received signal is also described in these publications. The experimental setup for validating the temperature sensing capability of the antenna sensor as well as its wireless interrogation is presented in figure 2. The sensor package was placed inside the furnace so that the environment temperature could be precisely controlled**.** The wireless interrogator was realized by using a Vector Network Analyzer

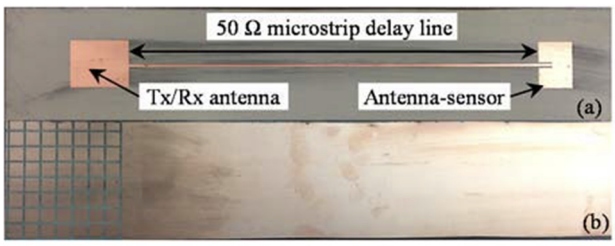

Figure 1. Passive wireless temperature sensor node fabricated from commercial high-temperature substrate; (a) top view (b) bottom view.

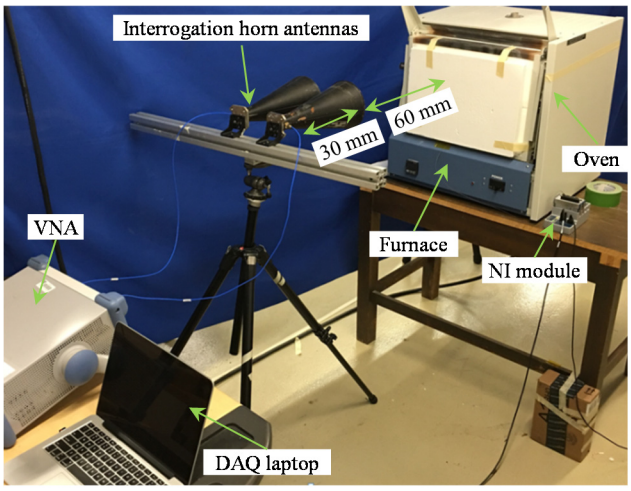

Figure 2. Experimental setup for characterizing the wireless antenna sensor inside an oven.

(VNA) and two horn antennas, which were placed at an interrogation distance of 60 cm in front of the temperature oven facing the Tx/Rx antenna. These two horn antennas were connected to the two-port VNA using coaxial cables so that the transmitting S-parameter (i.e., the S_{21} parameter) could be acquired. A T-type thermocouple was installed adjacent to the antenna sensor to obtain the reference temperature.

Results and discussions: The digital signal processing program converts the frequency domain S_{21} parameter to time domain, extracts the sensing signal by time-gating, and calculates its frequency spectrum. Figure 3a presents the frequency spectra of the time-gated signal at different temperatures. The resonant frequency of the antenna sensor is determined as the frequency at which the frequency spectrum has the lowest amplitude. Extracting the antenna frequencies at the various temperatures allows us to establish the temperature dependency of the antenna frequency as shown in figure 3b. The measurement data display a high degree of linearity (R^2 = 0.9984). The slope of the trend line is 195.13

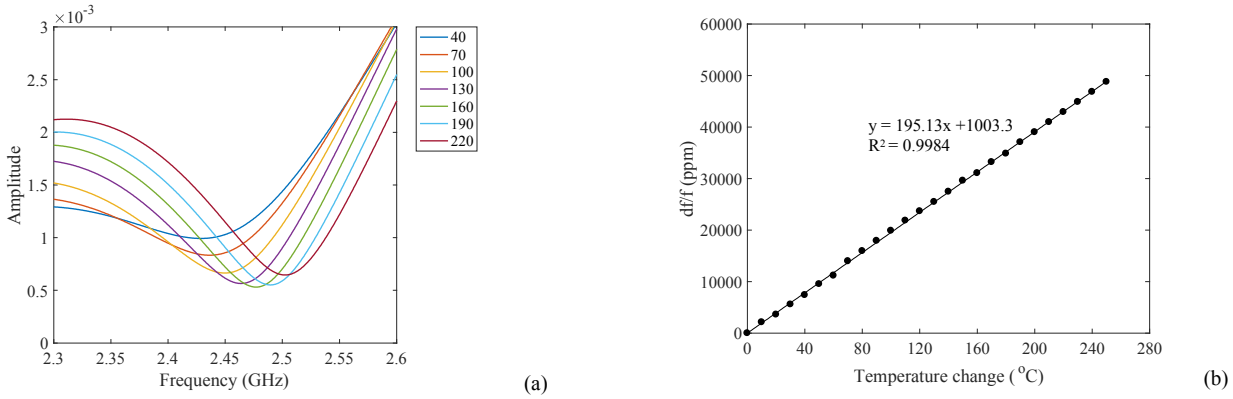

Figure 5. (a) Spectra of the gated time-domain signals at different temperatures; (b) The relationship between the measured normalized antenna frequency shift and temperature change.

ppm/°C, which is slightly higher than the simulated K_T value of 192.45 ppm/°C. The normalized deviation between the simulated and experimental K_T is 1.39%.

Conclusion: this study validated that an antenna sensor can be wirelessly interrogated without any electronics at the sensor node. It also validated that antenna sensors fabricated on commercial substrate can provide linear temperature measurements up to 270°C. This development could enable low-cost deployment of antenna sensors for various condition monitoring schemes. For more detailed discussions of results and conclusions, please refer to the publications listed above.

1.2. Wireless interrogation of distributed antenna sensor array

Experimental methods: to explore sensor multiplexing for distributed condition monitoring, we fabricated an antenna sensor array on a commercial high-temperature substrate (Rogers 3210). The antenna sensor array consists of two antenna sensors and they are frequency division multiplexed–i.e., each antenna sensor resonates at a district frequency for ease of identification. The sensors were designed to resonate at 2.63 and 3.34 GHz respectively. Figure 4 presents the fabricated antenna array using a chemical etching technique. Following the wireless interrogation mechanism described above, the antenna sensors were wirelessly interrogated using the experiment setup shown in figure 5.

Results and discussions: the time domain signal converted from the wirelessly measured S_{21} parameter is shown in figure 6a and the spectrum of the time-gated sensing signal is shown in figure

Figure 4. Wireless antenna sensor array fabricated using commercial high-temperature PCB.

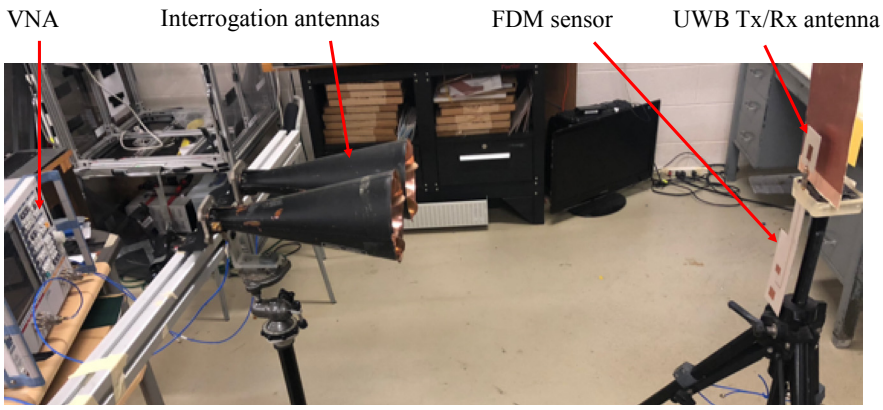

Figure 5. Experimental setup for characterizing the wireless antenna sensor array with two antenna sensors.

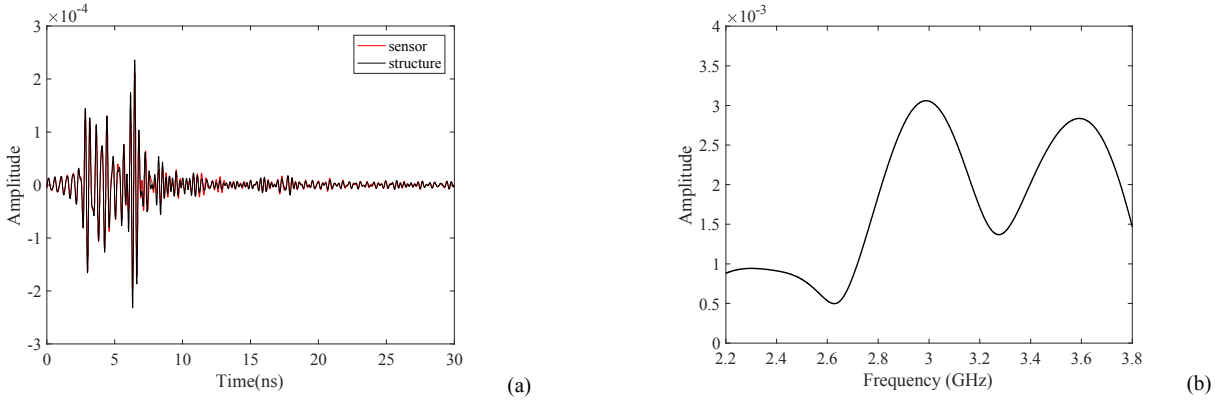

Figure 6. (a) Time domain signal converted from the measured S_{12} parameter of the wireless antenna sensor array; (b) spectrum of the gated time-domain signal with two valleys corresponding to the resonant frequencies of the two antenna sensors in the array.

6b. The antenna frequencies are determined from figure 6b as 2.64 and 3.33 GHz, which matched well with the frequencies measured using wired means.

Conclusion: the antenna frequencies measured using the wireless means agree perfectly with those obtained by wired measurements, and thus validate wireless interrogation of an antenna array by frequency division multiplexing. While the demonstration was carried out using two antenna sensors, more antenna sensors can be added based on the frequency multiplexing principle since the antenna sensors typically have narrow bandwidths.

2. Developed compact interrogators for dynamic interrogation of wireless antenna sensors

Publications:

J. Yao "Dynamic wireless interrogation of antenna-sensor in harsh environment," PhD dissertation, *2016*.

The instrument we used for task 1 (i.e., a VNA) is expensive, bulky and has a low sampling speed. To reduce the cost of the sensing system and to improve the mobility, we developed a compact, low-cost wireless interrogator based on the principle of Frequency Modulated Continuous Wave (FMCW) radar and demonstrated it for dynamic interrogation of the antenna sensor. The FMCW-based wireless interrogator provides substantial improvements on the interrogation speed and thus enables dynamic interrogation of the antenna sensors.

Experimental methods: figure 7(a) illustrate the circuit diagram of the FMCW interrogator. A down-conversion RF mixer was implemented in the interrogator circuit to demodulate the signal backscattered by the antenna sensor, which includes the sensing signal as well as the background clutter. Due to the time delay between the sensing signal and the background clutter, these two signals possess different beat frequencies in the down-converted signal. As such, they can be easily separated using a

band pass filter. The wireless interrogation system was first implemented using connectorized laboratory instruments as shown in Figure 7(b). The accuracy of the interrogator was validated using an antenna temperature sensor. After validated the performance of the system, a compact FMCW signal source was designed and implemented to reduce the size of the interrogator and thus increase its mobility. Figure 7(c) presents the implementation of the FMCW signal source on a circuit board using surface-mount components.

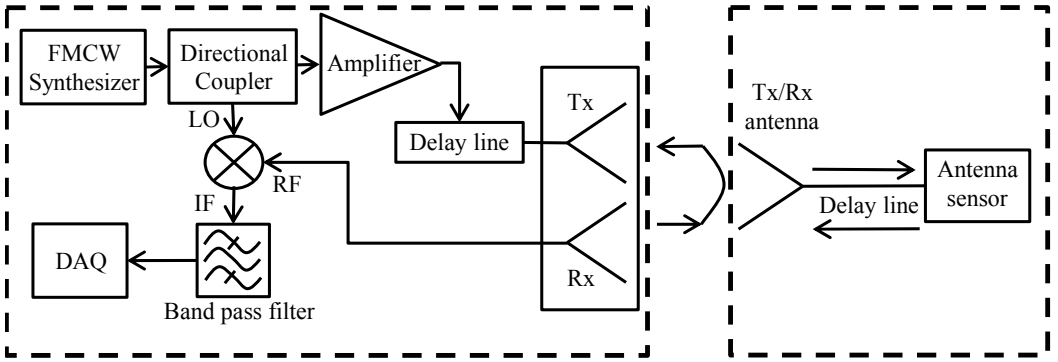

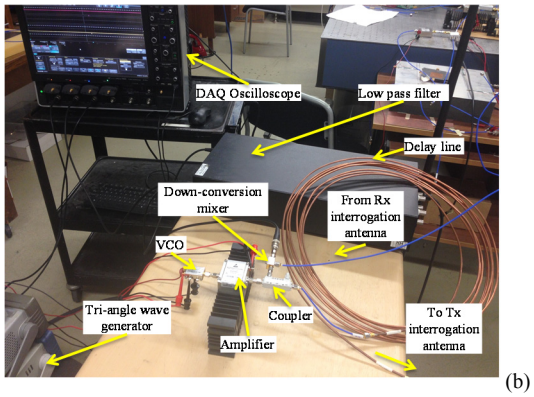

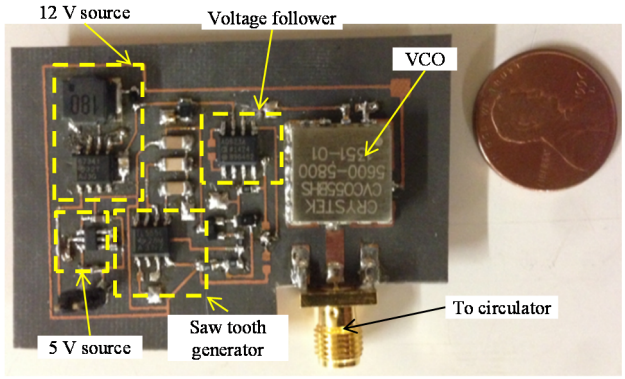

Figure 7. A custom-developed FMCW interrogator for dynamic interrogation of wireless antenna sensor: (a) circuit diagram; (b) hardware implementation; (c) hardware implementation of a compact FMCW source.

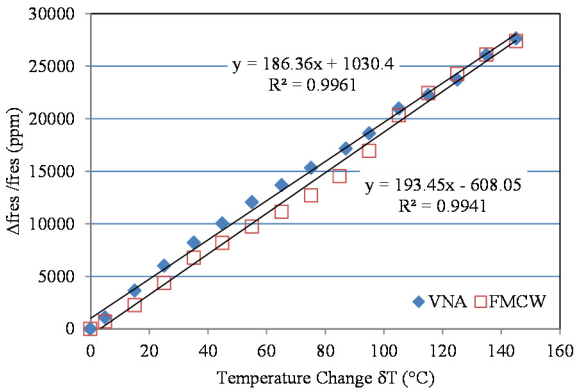

Figure 8. Comparison between frequency shift-temperature relationships measured using a VNA as the interrogator and the FMCW interrogator.

Results and discussions: a high interrogation speed of 50 Hz was achieved for the wireless interrogation system shown in Figure 7(b). A comparison between the measurements obtained using the FMCW interrogator and the VNA is shown in figure 8. The FMCW interrogator produced comparable results as those measured by a VNA.

The power consumption of the FMCW signal source was characterized to be only 160 mw and the interrogation rate is up to 55 Hz. Tests were performed to validate the accuracy of the proposed compact FMCW interrogator and the experimental results were compared with those from the network analyzer measurements. The normalized discrepancies of two measurements are within 0.002%.

Conclusions: this study demonstrates that the antenna sensors can be wirelessly interrogated using a custom-developed interrogator that is much cheaper, more compact, and has a faster interrogation speed than a high end laboratory instrument. Such an interrogator reduces the size and cost of the sensing system substantially and extends the functionality of the antenna sensor from static to dynamic measurements (e.g., vibration).

3. Investigate simultaneous measurements of multiple measurands using a single antenna sensor

Publications:

F. Tchafa, and H. Huang, "Microstrip patch antenna for simultaneous strain and temperature sensing", *Smart Mater. Struct.*, vol. 27, no. 6, pp. 2629-2636, 2018.

F. Tchafa, and H. Huang, "Microstrip patch antenna for simultaneous superstrate thickness and temperature sensing", under revision, *Smart Mater. Struct.*

F. Tchafa, H. Huang, "Simultaneous strain and temperature sensing using a single microstrip patch antenna", International Workshop on Structural Health Monitoring, September 12-14, 2017, Stanford University, California.

For the safe and efficient operation of coal-burning boilers, we identified three key measurands–temperature, strain, and ash thickness–that must be extracted from the antenna sensor response. In this study, we investigated dual-frequency antenna sensors for simultaneous strain and temperature sensing as well as temperature and ash accumulation measurements.

3.1. Simultaneous temperature and strain measurements

Experimental methods: the theoretical relationship between the antenna resonant frequency shifts, the temperature, and the applied strain was first established to guide the selection of the dielectric substrate, based on which an antenna sensor with a rectangular radiation patch was designed and fabricated. A tensile test specimen instrumented with the antenna sensor was subjected to thermo-mechanical tests inside an oven mounted on a mechanical tester, as shown in figure 9(a). For reference,

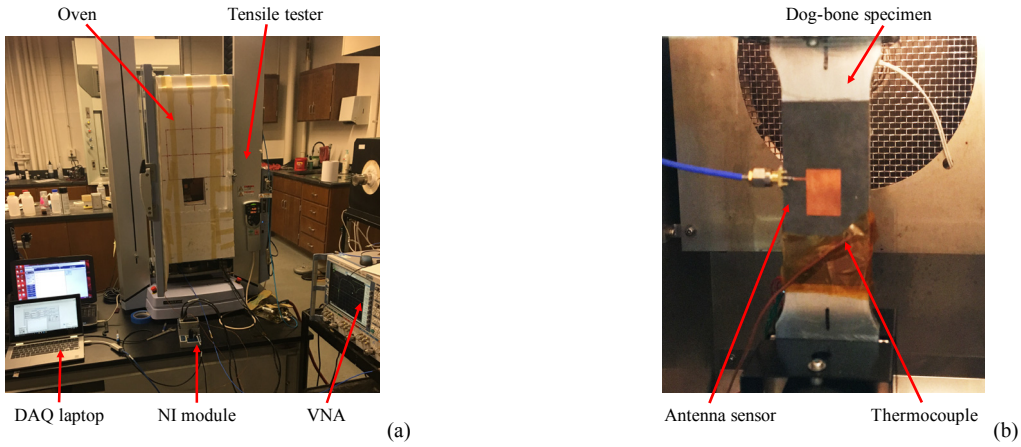

Figure 9. (a) Experimental setup for thermo-mechanical testing of the fabricated antenna sensor (b) dog-bone specimen with bonded antenna sensor and thermocouple.

the tensile test specimen was also instrumented with a conventional strain gauge and thermocouple, as shown in figure 9(b). The responses of the antenna resonant frequencies to strain or temperature variations, while keeping the other parameter constant, were first evaluated. Subsequently, the shifts of the antenna resonant frequencies under a combination of strain and temperature changes were characterized. A procedure was developed to inversely determine the temperature and strain conditions based on the antenna resonant frequencies and the extracted values were compared with the measurements provided by the strain gauge and thermocouple to assess the measurement uncertainties.

Results and discussions: as shown in figure 10, the S_{11}-paramter of the antenna sensor shifted left with the increase of strain under constant temperature and shifted right with the increase of temperature while keeping the strain constant. The variations of the antenna resonant frequency with the temperature and strain changes are shown in figure 11. It validated that the normalized antenna resonant frequency shifts vary linearly with the applied strain and temperature. Figure 12 shows the differences between the temperatures and strains inversely determined from the normalized frequency shifts and those measured

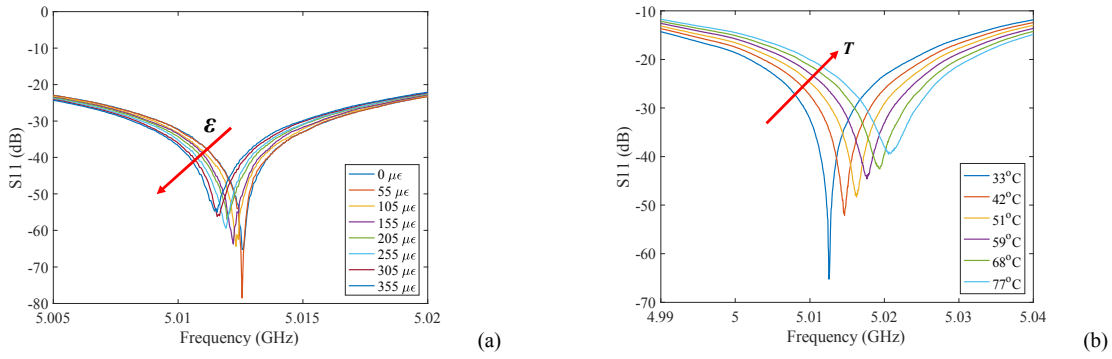

Figure 10. Measured S_{11} parameters of the TM010 mode: (a) the effect of strain at a constant temperature; (b) the effect of temperatures at a constant strain.

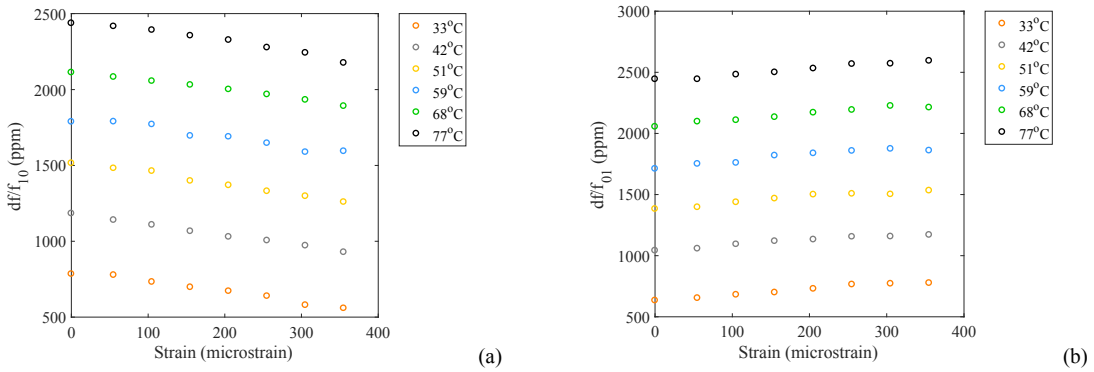

Figure 11. The normalized antenna frequency shifts with the applied strains under different temperatures; (a) f_{10} frequency and (b) f_{01} frequency.

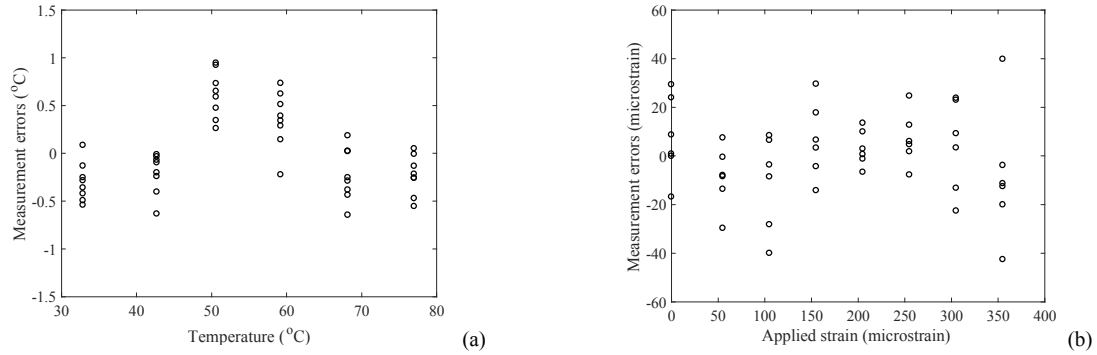

Figure 12. Differences between (a) temperature and (b) strain inversely determined from the normalized frequency shifts and those measured using a thermocouple and strain gauge, respectively.

using a thermocouple and strain gauge, respectively. One standard deviation yields measurement uncertainties of ±0.4°C and ±17.22 με for temperature and strain measurements, respectively.

Conclusions: by taking advantage of a dual-frequency antenna sensor, we established a procedure to extract two parameters simultaneously from one sensor measurement. This approach resolved the long-standing challenge of strain-temperature cross-sensitivity and thus enable temperature-compensated strain measurements. For more details about the methodology and results, please refer to the attached publications.

3.2. Simultaneous measurement of temperature and superstrate thickness

When ash accumulates on top of the antenna sensor, it serves as the superstrate for the antenna sensor. Thus, its thickness can be measured from the antenna resonant frequency shift. In this study, we demonstrated the use of microstrip patch antennas for measuring the ash thickness and temperature at the same time. As by-products, the dielectric constant of the ash and its temperature dependency are characterized as well.

Experimental methods: figure 13 illustrates a microstrip patch antenna temperature sensor covered with a dielectric layer (a.k.a. the superstrate). The superstrate changes the effective dielectric constant of the antenna sensor and thus its resonant frequencies. Meanwhile, temperature also influences the antenna frequencies because of the thermal expansion of the conductors, including the radiation patch and ground plane, and the TCD_k of the dielectric materials. Since a rectangular patch antenna has two fundamental frequencies, it enables determining these two parameters simultaneously. Once the temperature and superstrate thickness are determined, the dielectric constant of the superstrate and its temperature dependency can also be extracted. To demonstrate this capability, a dual-frequency patch antenna was designed, fabricated, and characterized with a superstrate of various thickness and at different temperatures. Figure 14 presents the antenna sensor fabricated on commercial high-temperature substrate (Rogers 3210) using a print-etching technique and the experimental setup for characterizing the antenna sensor. Ash layers with controlled thickness were deposited on top of the antenna sensor and the responses of the antenna resonant frequency to ash thickness changes under different temperatures were characterized. The relationship between the antenna resonant frequency shifts, ash thickness, and

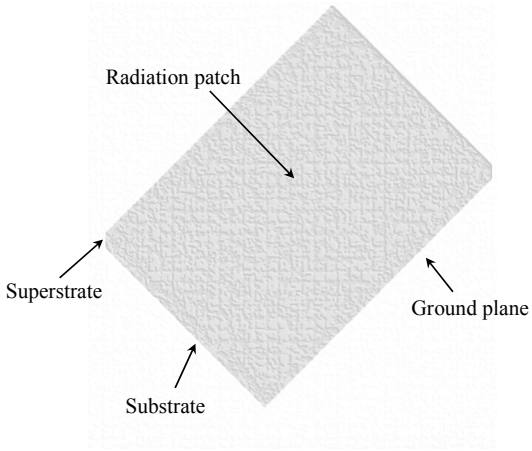

Figure 13. Illustration of a microstrip patch antenna temperature sensor covered with a superstrate.

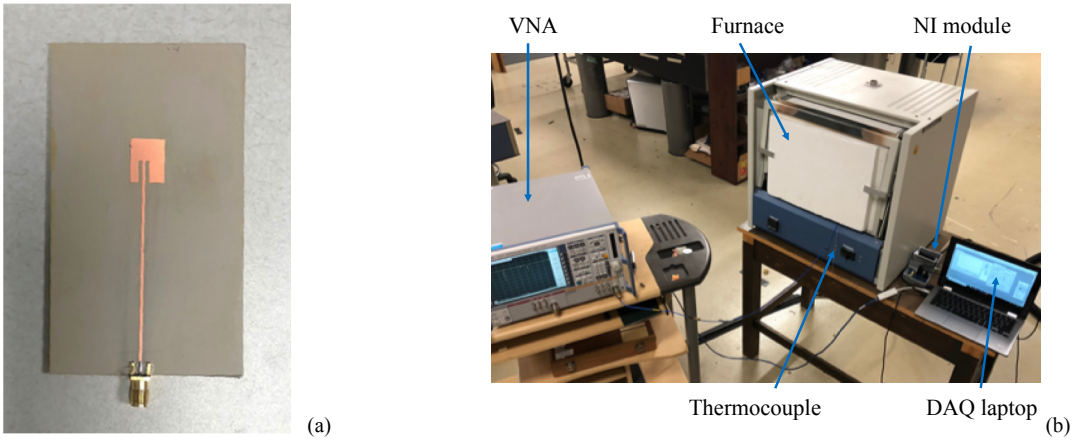

Figure 14. (a)Antenna sensor fabricated on Rogers 3210 printed circuit board (PCB) using a print-etching technique; and (b) experimental setup for characterizing the antenna sensor.

temperature was first establishing from the measurements using nonlinear regression algorithm. Based on this relationship, the ash thickness and temperature can be inversely determined from the antenna resonant frequency shifts. In addition, the dielectric constant of the ash layer at different temperature was determined by correlating the measured thermal response of the antenna sensor with simulations. As a result, the temperature dependency of the ash dielectric constant was characterized.

Results and discussions: the measured antenna frequencies to the simultaneous effects of temperature and ash accumulation are plotted in figure 15a and 15b. The f_{10} and f_{01} antenna frequencies decreased with ash build-up under constant temperature but the relationships are not linear. At constant ash thickness, the f_{10} and f_{01} antenna frequencies increased linearly with an increase in temperature. By fitting the antenna resonant frequencies as functions of the superstrate thickness and temperature, these two parameters were inversely determined from the measured antenna frequencies. Figure 16 presents a comparison between the ash thicknesses and temperatures inversely determined from the antenna sensor frequencies and the actual inputs (i.e., temperature and ash thickness). The measurement uncertainties were determined to be ±0.58°C and ±58.05 μm for temperature and superstrate thickness, respectively. The dielectric constant of the ash was found to be 2.64 at room temperature and its TCD_k was found to be 918 ppm/°C.

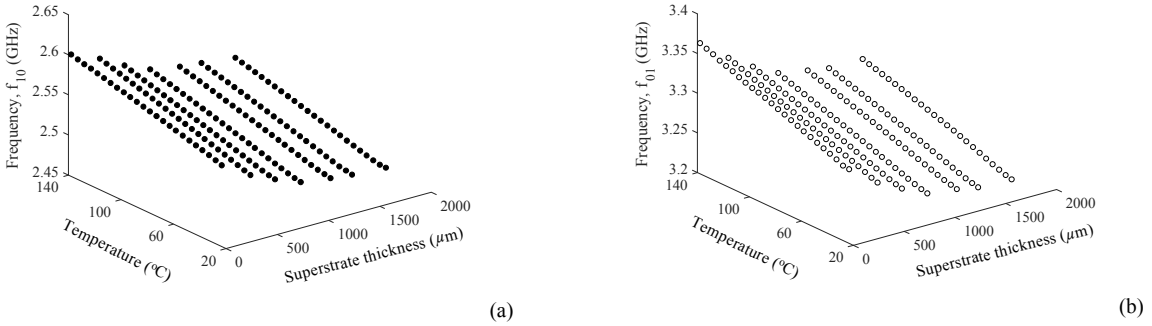

Figure 15. The measured effects of ash accumulation and temperature changes on the (a) f_{10} and (b) f_{01} frequencies of the antenna sensor.

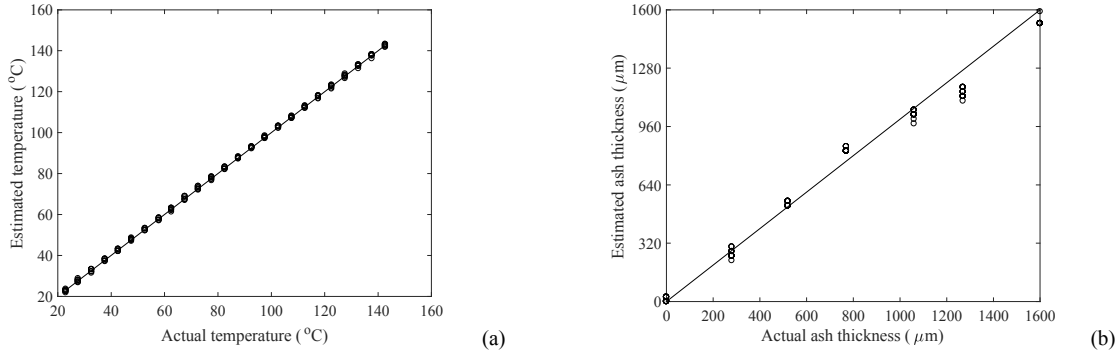

Figure 16. A comparison between ash thickness and temperature inversely determined from the antenna sensor frequencies and the actual inputs: (a) temperature, and (b) ash thickness.

Conclusions: the dielectric constant of ash is highly dependent of coal and the combustion condition, this study validated a methodology to measure the dielectric constant of ash under different temperatures and ash thicknesses. Potentially, this approach can be extended for monitoring the combustion process based on the changes in the dielectric constant of ash.

4. Fabricate antenna sensors from high-temperature materials

By removing electronics from the wireless sensor nodes, the maximum operating temperature of the antenna sensor is no longer limited by the electronics but the dielectric and conductive materials. In this study, we investigated implementing the antenna sensors using high-temperature materials. Platinum paste was tape casted on alumina substrates based on the designed patterns, followed by drying and firing. To control the dimension of the antenna pattern, laser machining was employed to trim the pasted pattern. In addition, sensor implementation using commercial metalized alumina substrates was also explored. The thermal response of the antenna sensor fabricated on alumina substrates was characterized.

4.1. Fabrication of antenna sensors using platinum paste and alumina substrate

Experimental Methods: designed patterns were cut on non-residual adhesive sheets. Commercially available alumina substrates were thoroughly cleaned with de-ionized water, followed by acetone, then isopropyl alcohol, and de-ionized water again as the final cleaning step. All cleaning steps were done in an ultrasonic cleaner. Afterwards, the substrates were fully dried in an oven. The patterned adhesive

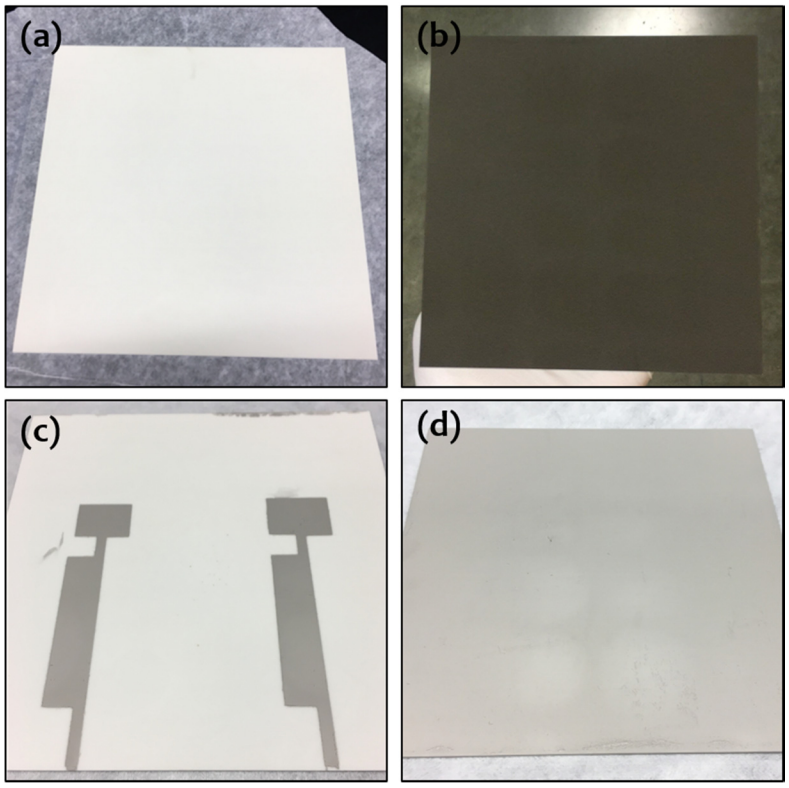

Figure 17. (a) Alumina substrate ultrasonic cleaned and dried; (b) dried platinum paste after 80°C overnight; (c) front patterns of platinum coating after firing; and (d) back electrode after firing.

sheets were carefully applied on the clean alumina substrate surface without trapping any bubbles inside. Alumina substrate was placed on the vacuum stage of the tape caster. Platinum paste was applied on the surface using a wide blade. After a smooth layer of platinum paste was applied on the alumina substrate, the sample was left on the stage and cured for 4 hours with a cover to prevent particles in the air from contaminating the platinum paste. In the next step, the adhesive mask was removed and the sample was dried at 80°C on the heating stage of the tape caster overnight. The sample was further dried in a furnace at 100°C for 10 minutes and fired at 1000°C for 10 minutes. The heating rate was controlled at 8°C/min in both ramping steps. Finally, the sample was cooled down with the furnace. Figure 17 shows the sample conditions at different steps of the experiment.

Defects on the sample surface were characterized using a white light interferometry surface profiler. As shown in figure 18, two kinds of defects were observed. In figure 18(a), there are scattered small pores presumably due to the sintering of platinum particles during the firing of platinum paste. In figure 18(b), a large pore was observed, this probably resulted from the paste inhomogeneity, or the dust on the alumina substrates before applying paste.

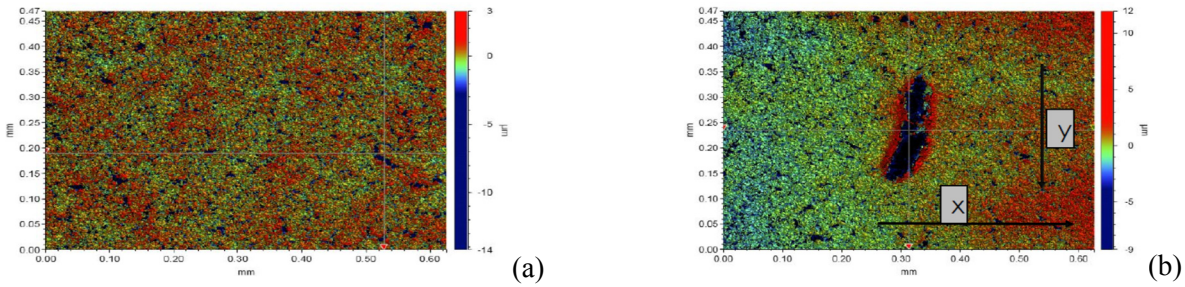

(a) (b)

Figure 18. Defects observed in fired platinum on an alumina substrate; (a) small pores and (b) a large pore.

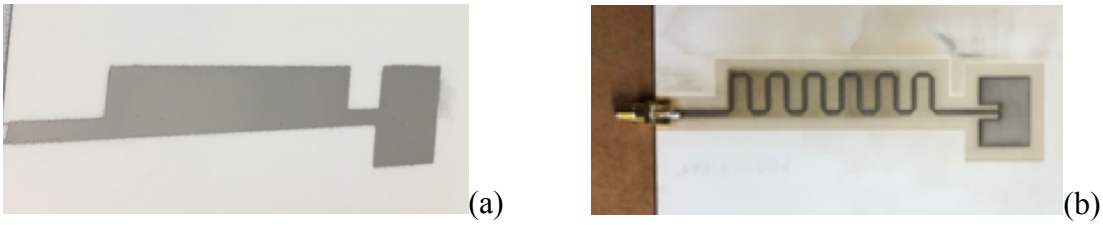

(a) (b)

Figure 19. High-temperature antenna sensor fabricated using alumina as the substrate and platinum as conductors: (a) before laser machining; and (b) after laser machining.

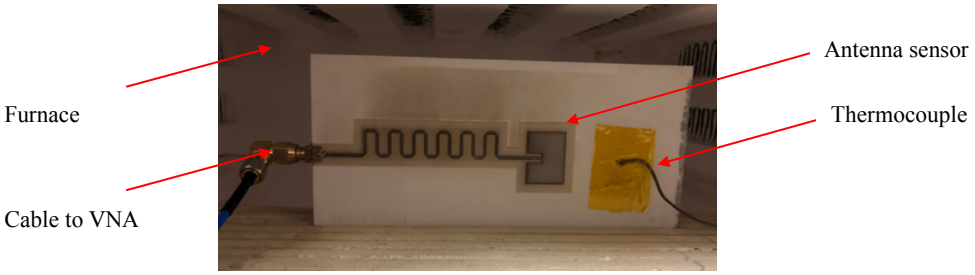

Figure 20. Experimental set up for thermal testing of a high-temperature antenna sensor fabricated on a 1.2 mm thick alumina substrate using platinum as the conductor.

Due to these defects, we added margins to the designed antenna pattern and used laser machining to trim the edges of the pasted pattern. Figure 19 shows the antenna sensor fabricated on alumina and platinum. As shown in figure 19a, the masked used to paste the platinum has a larger offset to accommodate for fabrication limiations. Laser machining was used to obtain the antenna sensor shape from the tape-casted platinum and the results are shown in figure 19b. The temperature sensitivity of the fabricated sensor was evaluated using the experiment setup shown in figure 20. An OMEGA T-type thermocouple was placed adjacent to the antenna sensor for temperature monitoring. The furnace was set to heat up at a rate of 2ºC/minute up to 150°C given the temperature limitation of the wire used for S_{11} measurments of the antenna sensor. The S_{11} parameters were acquired using a VNA set with a 10 kHz resolution.

Results and discussions: figure 21 presents the S-parameter measurements of the fabricated antenna sensor. The S_{11} parameter shown in figure 21a confirms that the antenna does resonate at 2.95 GHz, and it is in a good agreement with the design frequency of 3 GHz. Based on the S_{21} parameter shown in figure 21b, the gain of the antena sensor was measured to be 3.3 dBi – a significant improvement from previous measurements of -9 dBi without laser machining. Converting the measured S_{11} parameters to the time domain signal, we see that the sensor signal arrives at approximately 3.5 ns as shown in Figure 21c, and it is in good agreement with the design requirement of at least 3 ns of delay time.

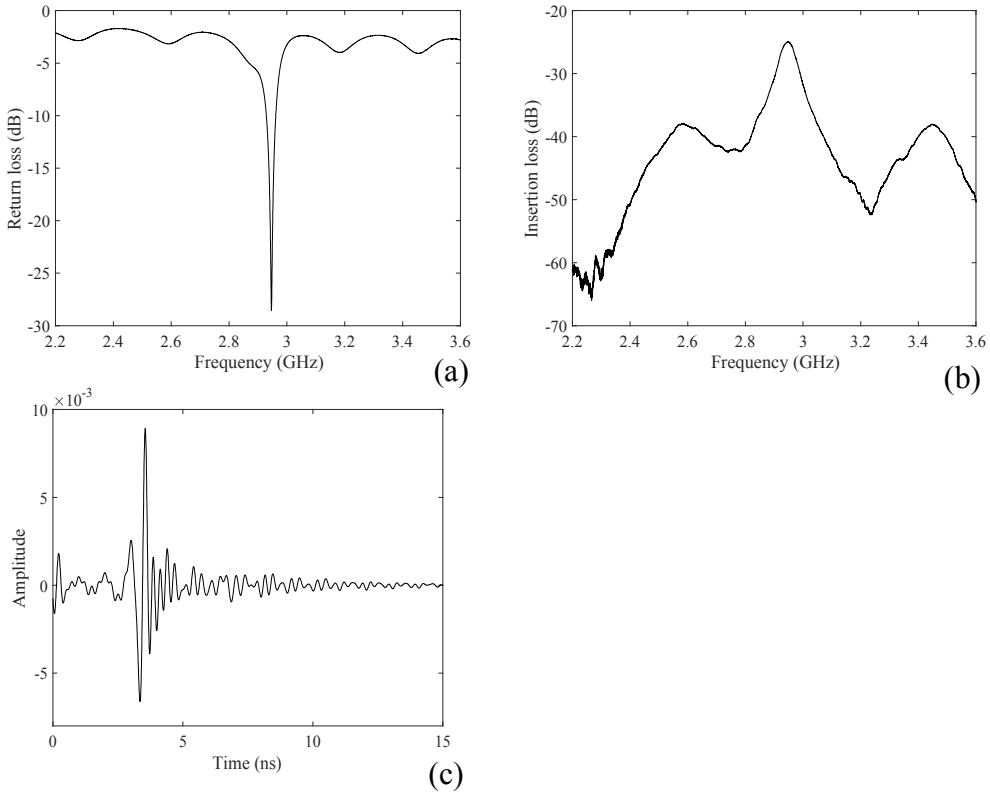

Figure 21. Characterization of the antenna sensor fabricated on an alumina substrate using platinum as conductor: (a) S_{11} measurement; (b) S_{21} measurement; and (c) time-domain representation of S11 measurement.

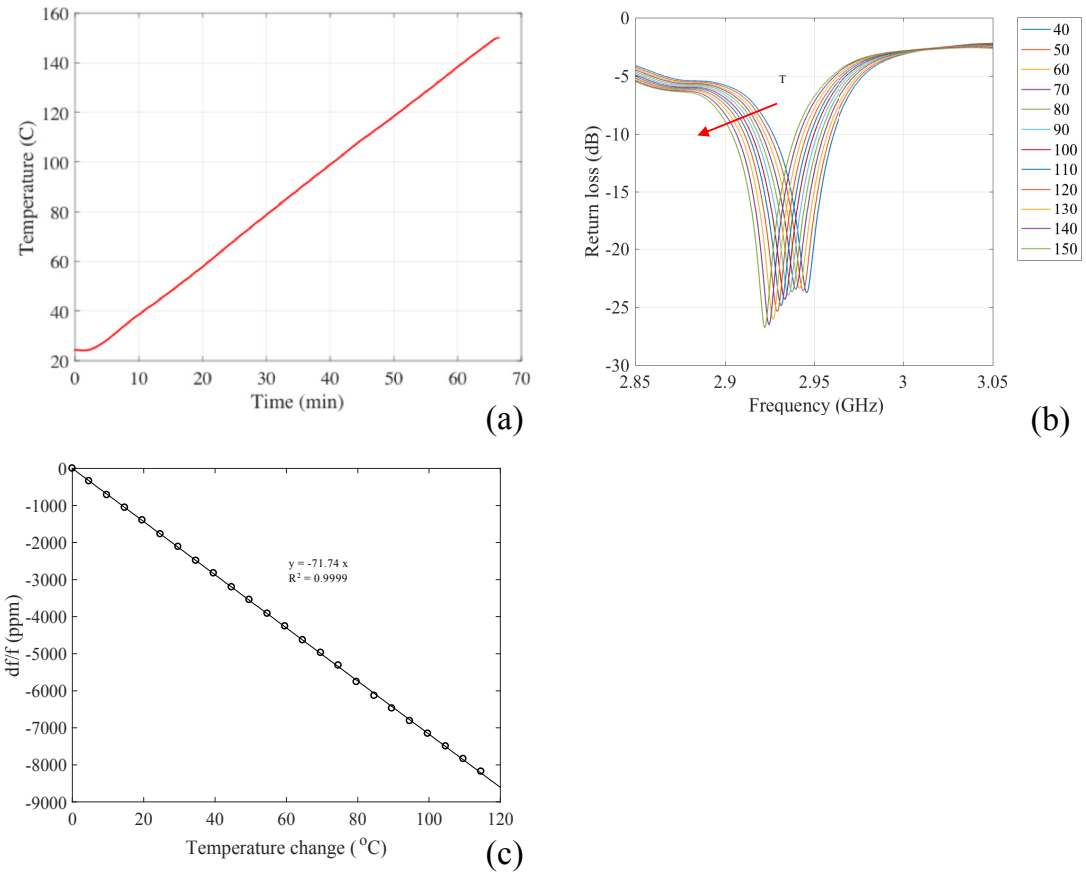

Figure 22. Experimental results obtained from antenna sensor fabricated from an alumina substrate and platinum paste: (a) thermocouple temperature reading; (b) effect of temperature on the S_{11} parameters of the antenna sensor; and (c) normalized resonant frequency shift with temperature.

Figure 22 presents the measurement results obtained from the thermal testing of the antenna sensor. As shown in figure 22a, the maximum temperature tested was 150ºC, again limited by the coaxial cable. As temperature increase, the S_{11} curves of the antenna sensor shift to the left; this indicates a decrease in the resonant frequency of the antenna sensor. Plotting the normalized frequency shift versus temperature in figure 22c, the measured temperature sensitivity is determined to be -71.71 ppm/ºC, corresponding to an extracted TCD_K of 127.5 ppm/ºC for the alumina susbtrate. The measurement displayed excellent linearity with an R^2 value of 0.9999.

Conclusion: antenna sensors were fabricated by tape casting platinum paste on alumina substrates. By controlling the experiment details carefully, samples with tolerable defects can be fabricated. To achieve precise antenna pattern, margins were added to the designed patterns and edges were smoothened by subsequent laser cutting. Thermal testing of the fabricated antenna sensor confirmed that the antenna resonant frequency shifted linearly with the temperature increase.

4.2. Fabrication of antenna sensors using commercial metalized alumina substrates

Although the antenna sensor was succesfully fabricated from high-temperature materials, the cost of the alumina substrates was relatively high and the yield of the tape casted platinum layer with tolerable defects was low. To reduce the fabrication cost, we explored commercial high-temperature printed circuit board for the antenna sensor implementation.

Experimental methods: Rogers Curamik was selected as the high-temperature commercial substrate for sensor implementation. It is made of Al_2O_3 with a coefficient of thermal expansion of 6.8 ppm/K specified in the 20-300ºC range. The dielectric constant of the substrate is 9.8. The sensor was designed to operate at a frequency of 2.5 GHz and has a transmission line designed to provide 3.5 ns delay to separate the sensing signal from the background clutter. Given the desired resonant frequency and the parameters of the available susbtrate, the sensor dimensions were designed to be 19 by 26 mm^2 (see Figure 23). The sensor was fed by a 50 Ohm microstrip transmission line with a trace width of 1 mm. Since the substrate is only available in the size of 5.5 by 7.5 in^2, we used a meandering transmission line rather than a straight transmission line to ensure the required delay could be provided. The edges of the meandering line were chamfered to avoid discontinuities. Figure 23 presents the dimensions of the antenna sensor as well as the meandering line. Figure 24a and 24b show the simulated S_{11}-parameter of the sensor and its corresponding time-domain signal, respectively. The simulated antenna frequency and its arrival time of 3.5 ns agree well with the initial design. The sensor was fabricated and subjected to temperature up to 120ºC so its temperature sensitivity could be determined. In theory, the normalized resonant frequency shift of the antenna sensor depends on the TCDk and the coefficient of thermal expansion (CTE), i.e. df/f = - (TCDk/2 + CTE) dT. Since the substrate manufacturer didn't provide the TCDk value, it had to be extracted experimentaly. To ensure the sensitivity of the antenna sensor could be accurately captured, a literature search was conducted. It revealed that there wasn't any definite value for the TCDk for alumina as it also depends on the manufacturing process and the purity of alumina. However, all literature showed that the TCDk of alumina is positive. With a CTE of 6.9 ppm/ºC, we expect at least -35 ppm frequency shift for a 5ºC change. With a design frequency of 2.5 GHz, this is

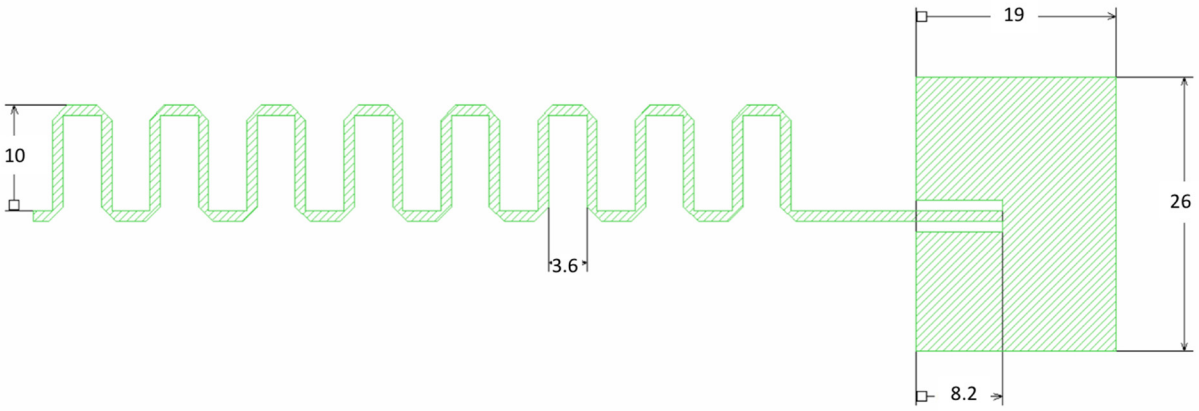

Figure 23. Design of a 2.5 GHz antenna sensor on a 1 mm thick alumina substrate with a copper conductor.

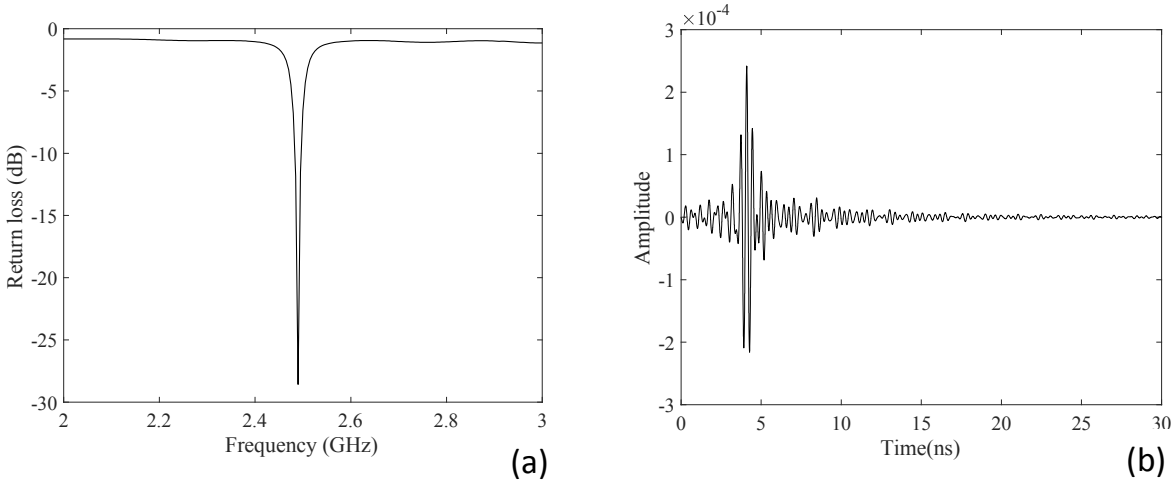

Figure 24. Simulated results of antenna sensor designed on an alumina substrate with a copper conductor: (a) S_{11} parameters; (b) time-domain representation of the S_{11} parameters.

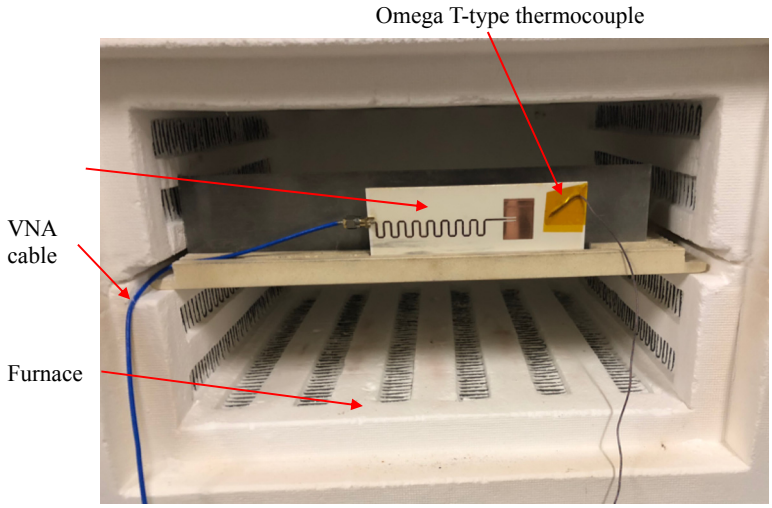

Figure 25. Experimental set up for thermal testing of an antenna sensor fabricated from commercial metalized alumina substrate Curamik.

equivalent to more than 90 kHz frequency change. Therefore, the VNA resolution was set to have a resolution of 10 kHz. Figure 25 presents the experimental set up to determine the temperature sensitivity of the antenna sensor fabricated on Curamik. Temperature was measured using a T-type thermocouple from OMEGA. The S_{11} parameters were acquired using a VNA set to sweep from 2.38 GHz to 2.68 GHz with a frequency resolution of 10 kHz. The furnace was set to heat up the sensor at a rate of 2°C/minute.

Results and discussions: Figure 26 presents the experimental results. The measurements display excellent linearity with an R^2 value of 0.9999. The temperature sensitivity of the antenna resonant frequency was measured to be -63.59 ppm/°C. This corresponds to a TCDk of 114 ppm/ °C over the measured range. The measurement error is ±0.3°C and it is well within the thermocouple error of ±0.5°C.

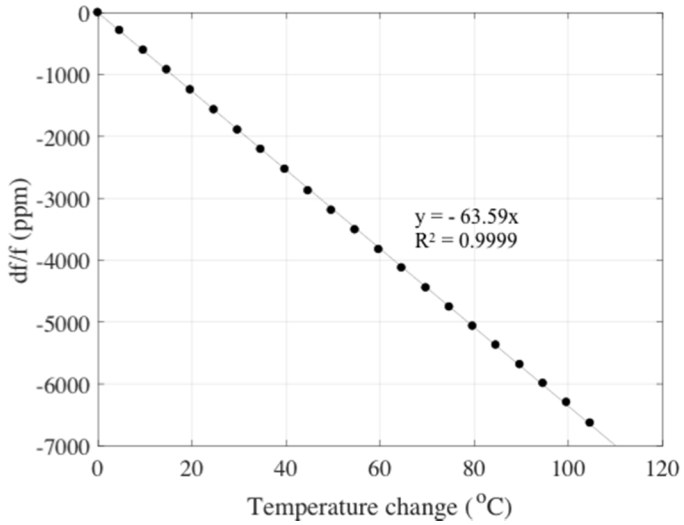

Figure 26. Linear relationship between the normalized resonant frequency shift and temperature, obtained from the antenna sensor fabricated on commercial metalized alumina substrate Curamik.

Conclusions: we have fabricated antenna sensors on alumina substrates either using platinum paste or commercial metallization and characterized the temperature response of the antenna resonant frequency using wired connections. In both cases, a linear relationship between the temperature and antenna resonant frequency was validated. We will finalize the design of the UWB TxRx antenna on Curamik to demonstrate wireless sensing using the antenna sensor at higher temperatures.

Products

a. Publications

Journal publications

1. F. Tchafa, and H. Huang, "Microstrip patch antenna for simultaneous superstrate thickness and temperature sensing", manuscript *submitted to IOP Smart Mater. Struct.*
2. F. Tchafa, and H. Huang, "Microstrip patch antenna for simultaneous strain and temperature sensing", *Smart Mater. Struct., vol. 27, no. 6, pp. 2629-2636, 2018.*
3. J. Yao, F. Tchafa, H. Huang, "Far-field interrogation of patch antenna for temperature sensing without electronics", *IEEE Sens. J., vol. 16, no. 19, pp. 7053–7060, 2016.*

PhD dissertations

1. F. Tchafa, "Wireless antenna sensors for boiler condition monitoring," PhD in Mechanical and Aerospace Engineering, University of Texas Arlington, 2018.
2. J. Yao "Dynamic wireless interrogation of antenna-sensor in harsh environment," PhD in Electric Engineering, University of Texas Arlington, 2016.

Other publications, conference papers and presentations

1. F. Tchafa, H. Huang, "Simultaneous strain and temperature sensing using a single microstrip patch antenna", *International Workshop on Structural Health Monitoring, September 12-14, 2017, Stanford University, California.*
2. F. Tchafa, J. Yao, H. Huang, "Wireless interrogation of a high-temperature antenna sensor without Electronics", *International Mechanical Engineering Congress and Exposition, November 11-17, 2016, Phoenix, Arizona.*

b. Web site

The website of the PI's group can be assessed by http://astl.uta.edu/Research.htm and it contains information about this project.

c. Collaborations

This project was jointly carried out by researchers from the University of Texas Arlington and University of California San Diego. In addition, the PI has discussed with Signal Pro LLC, a company located at Silver springs, MD about exploring commercialization opportunities of the developed technologies. The PI was invited to visit the Department of Chemical and Biomedical Engineering at West Virginia University by Professor Debangsu Bhattacharyya and had productive discussions with Professor Edward Sabolsky on exploring conductive ceramics for sensor implementation.

d. Technologies/Techniques

1. Passive wireless antenna sensors that can be interrogated without electronics at the sensor node;
2. Frequency division multiplexing scheme to realize sensor arrays with multiple antenna sensors;
3. FMCW-based wireless interrogation circuit/unit that can perform wireless dynamic interrogation of the antenna sensors;
4. Algorithm and procedure to inversely extract multiple measurands simultaneously from one sensor response;
5. Techniques for measuring the dielectric constant of materials placed on top of the antenna sensor and its temperature dependency;
6. Fabrication procedures for producing antenna sensors from high-temperature materials.

e. Inventions/Patent Applications, licensing agreements

None.

f. Other products, such as data or databases, physical collections, audio or video, software or netware, models, educational aid or curricula, instruments or equipment.

None.

MILESTONE STATUS REPORT

Milestone title/description	Planned Completion Date	Actual Completion Date	Verification Method
1. Demonstrate wireless interrogation of passive antenna sensors	8/31/2015	9/30/2015	Journal paper published
2. Demonstrate the fabrication of flexible dielectric substrates	10/31/2015	12/31/2015	Test commercial substrate at temperature up to 270^{o}C
3. Demonstrate temperature chamber	3/31/2016	12/31/2015	Used for sensor characterization
4. Demonstrate nonlinear regression algorithms for multi-modality sensing	7/31/2016	11/15/2018	One journal paper published and one journal manuscript under review
5. Finalize material recipe	9/30/2016	12/1/2018	Antenna sensor completed. UWB Tx/RX antenna designed
6. Demonstrate distributed antenna sensor array	6/30/2017	9/1/2018	Experimental validation

Far-Field Interrogation of Microstrip Patch Antenna for Temperature Sensing Without Electronics

Jun Yao, *Student Member, IEEE*, Franck Mbanya Tchafa, *Student Member, IEEE*, Ankur Jain, Saibun Tjuatja, *Senior Member, IEEE*, and Haiying Huang, *Member, IEEE*

***Abstract*— Temperature sensing without electronics is demonstrated through wireless interrogation of passive antenna-sensors. The sensor node is equipped with an ultra-wide-band microstrip antenna as the transmitting/receiving (Tx/Rx) antenna and a microstrip patch antenna serving as the temperature-sensing element. A microstrip transmission line connecting the Tx/Rx antenna and the antenna-sensor delays the signal reflected from the sensing element and thus separated it from the background clutter. The operation principle of the wireless sensing scheme is first discussed, followed by the design and simulations of the sensor node circuitry. A digital signal processing algorithm that extracts the antenna resonant frequency from the wirelessly received signal is also described. Temperature tests were conducted to validate the performance of the wireless antenna sensor inside an oven.**

***Index Terms*— Wireless interrogation, passive wireless sensor, temperature sensor, UWB antenna, antenna-sensor, condition monitoring.**

I. Introduction

TEMPERATURE sensing is important inside many industrial production environments to optimize their operation parameters and to ensure safety. Due to their harsh environments, conditioning monitoring of these machines is extreme challenging. Wired temperature sensors, such as thermocouples [1] and optical fiber sensors [2] are commonly used. However, cables and connectors that can sustain high temperatures are expensive and prone to failure [3]. Various wireless temperature sensing techniques have been developed in recent years to eliminate the wiring requirements. Base on their configurations, wireless temperature sensors can be classified into two categories: the ones with electronic chips on board (i.e. the chip-based wireless sensors) or the ones without any electronic chips (i.e. the chipless wireless sensors). Most chip-based wireless sensors are designed based on the Berkeley mote platform [4], in which a microcontroller controls the data acquisition, signal processing, as well as the wireless data transmission [5], [6]. As such, these wireless sensors also need an on-board battery to power the microcontroller and the associated peripherals. Another group of chip-based wireless sensors is based on the Radio Frequency Identification (RFID) technology. A Wireless Identification and Sensing Platform (WISP) were presented in [7]. Similar to the mote-based wireless sensors, the WISP acquires the analog outputs of external sensors and converts them into digital data. The digital sensing data are then wirelessly transmitted by modulating the backscattered interrogation signal. As such, the WISP does not have a wireless transmitter on board and thus can operate on energy harvested from the interrogation signal. The power consumption of the RFID-based temperature sensors can be further reduced by implementing a complementary metal-oxide semiconductor (CMOS) temperature sensor that directly modulates the backscattered signal without any digitization [8]. One common limitation of the chip-based wireless sensors is that they can only operate at temperatures below the temperature limit of the electronic chips. At higher temperatures, chipless wireless sensors are the only feasible solution. Reindl and Shrena [9] demonstrated a remote temperature sensing system using a Surface Acoustic Wave (SAW) sensor and a passive dipole antenna, in which a radio frequency (RF) signal is received by the antenna and passed on to an interdigital transducer (IDT) to generate SAWs in the piezoelectric substrate. A reflector placed at a distance from the IDT reflects the SAWs back to the IDT, which is subsequently converted to RF signals and retransmitted by the dipole antenna. Temperature is then measured from the SAW speed that is extracted from the wirelessly received signal. The low operation frequency of the SAW sensors, however, makes sensor miniaturization extremely difficult. Chipless RFID sensors are another alternative for passive wireless temperature sensing. In [10], a resistive temperature sensor was implemented as the load of a UWB antenna. Due to the impedance mismatch between the resistive load and the antenna, the amplitude of the antenna backscattering is modulated as a function of temperature. Unfortunately, the antenna backscattering is also influenced by the distance and orientation between the reader and the sensor. Therefore, it is difficult to achieve calibrated sensor measurements using such a configuration. Self-calibrated wireless temperature sensor was achieved by connecting an RF cavity resonator to an antenna and temperature can be measured from the shift of the resonant frequency using a time-domain (TD) gating technique [11]. A dielectric resonator made of zirconium tintitanate was also studied for wireless temperature sensing [12]. Since the resonator can retain a Quality (Q) factor higher than 670 at 700 °C, far-field sensing of its resonator frequency up to 1.2 m was achieved. The major limitation of a dielectric resonator is that its Q factor decreases

Manuscript received June 21, 2016; accepted July 26, 2016. Date of publication August 2, 2016; date of current version September 1, 2016. This work was supported by the Department of Energy under Award DE-FE0023118. The associate editor coordinating the review of this paper and approving it for publication was Prof. Boby George.

J. Yao and S. Tjuatja are with the Department of Electric Engineering, University of Texas at Arlington, Arlington, TX 76019 USA (e-mail: jun.yao@mavs.uta.edu; tjuatja@uta.edu).

F. Mbanya Tchafa, A. Jain, and H. Huang are with the Department of Mechanical and Aerospace Engineering, University of Texas at Arlington, Arlington, TX 76019 USA (e-mail: franckeric.mbanyatchafa@mavs.uta.edu; jaina@uta.edu; huang@uta.edu).

Digital Object Identifier 10.1109/JSEN.2016.2597739

as the temperature increases [12], [13]. Thus, the radiated power from the resonator decays quickly at higher temperatures, which makes far-field sensing difficult. Besides, a dielectric resonator is usually quite bulky. Another chipless wireless temperature sensor is the coupled Inductive-Capacitive (LC) resonance sensor [14], [15]. Temperature affects the resonant frequency of the LC sensor and its frequency can be wirelessly detected via inductive coupling between the sensor and the reader coils. The interrogation distance of LC resonant sensors, however, is only a few centimeters since the coils of the sensor and reader have to be placed in the near fields of each other.

Significant researches have been conducted on the antenna-sensor technology due to its planar configuration, low-cost, passive operation, and multi-modality sensing capabilities [16]. Since the antenna-sensor has a simple and conformal planar configuration, it can be easily attached on the structure surfaces for Structure Health Monitoring (SHM) [17]. Several wireless interrogation techniques have been developed for the antenna sensors, including normalized Time Domain Reflectometry (TDR) [18] and RFID-enabled techniques [19]–[21]. High-speed wireless interrogation of the antenna-sensor was achieved using an amplitude modulator and a Frequency Modulated Continue Wave (FMCW) interrogator [22]. Similar to the RFID sensors, the wireless interrogation mechanisms developed so far require electronics in the sensor node, which limits their applications in high-temperature environments. In order to use an antenna-sensor for high temperature sensing, wireless sensor nodes without electronics have to be developed. A near-field interrogation mechanism for a chipless antenna-sensor was proposed in [23]. The patch antenna-sensor was directly interrogated without using any electronics. However, since the patch-antenna has a relative low Q factor [24], the maximum wireless interrogation distance achieved was only 5 cm.

In this study, far-field interrogation of an antenna-sensor without electronics was demonstrated for temperature sensing. The sensor node consists of a microstrip patch antenna serving as the temperature sensing unit [25] and a UWB transmitting/receiving (Tx/Rx) antenna with a Reactive Impedance Surface (RIS) ground plane [26], [27]. While other passive wireless sensors usually have an antenna as a data communication device, to the best of our knowledge, the presented work is the first in employing the microstrip antenna as a wireless temperature sensing element. By doing so, the entire sensor node can be implemented on a commercial printed circuit board (PCB) using simple fabrication techniques such as chemical etching. The temperature information is encoded in the signals backscattered by the antenna sensor and a TD gating technique is developed to extract the resonant frequency of the antenna sensor from the backscattered signal.

II. Principle of Operation

A. Patch Antenna for Temperature Sensing

Assume a rectangular patch antenna operates in the TM_{010} mode, its resonant frequency f_{res} can be calculated based on the transmission line model [28], i.e.

$$f_{res} = \frac{c}{2L_e\sqrt{\varepsilon_r}}, \tag{1}$$

where c is the speed of light and ε_r is the dielectric constant of the substrate material. L_e is the electrical length of the patch antenna, which equals to the physical length L of the radiation patch approximately, i.e. $L_e \approx L$. The resonant frequency variation δf_{res} can then be expressed in terms of the changes in the substrate dielectric constant ε_r and the patch length L as

$$\delta f_{res} = \frac{\partial f_{res}}{\partial \varepsilon_r}\delta\varepsilon_r + \frac{\partial f_{res}}{\partial L}\delta L. \tag{2}$$

We can also derive from equation (1) that

$$\frac{\partial f_{res}}{\partial \varepsilon_r} = \left(-\frac{1}{2\varepsilon_r}\right) f_{res} \tag{3}$$

and

$$\frac{\partial f_{res}}{\partial L} = \left(-\frac{1}{L}\right) f_{res}. \tag{4}$$

Substituting equations (3) and (4) into (2) and normalizing the resonant frequency shift with the antenna's resonant frequency, we obtain

$$\frac{\delta f_{res}}{f_{res}} = -\frac{1}{2}\frac{\delta\varepsilon_r}{\varepsilon_r} - \frac{\delta L}{L}. \tag{5}$$

For the purpose of temperature sensing, equation (5) can be expressed in terms of temperature change δT as

$$\frac{\delta f_{res}}{f_{res}} = -\frac{1}{2}\alpha_\varepsilon\delta T - \alpha_T\delta T = \left(-\frac{1}{2}\alpha_\varepsilon - \alpha_T\right)\delta T = K_T\delta T, \tag{6}$$

where α_ε is the thermal coefficient of the substrate dielectric constant; α_T is its coefficient of thermal expansion. K_T is defined as the temperature sensitivity of the normalized frequency shift and is a linear function of α_ε and α_T.

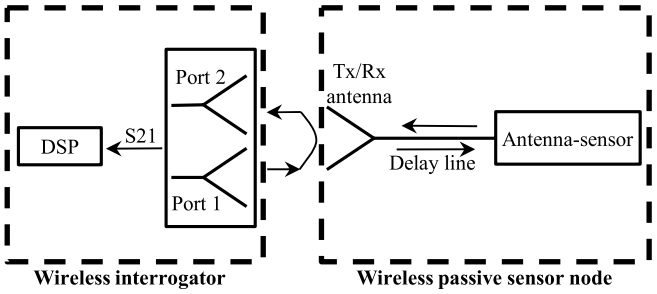

Fig. 1. Block diagram of the wireless temperature sensing system.

B. Wireless Interrogation Based on Antenna Backscattering

The wireless sensing system can be separated into two subsystems: a wireless interrogator and a passive wireless sensor node, as shown in Fig. 1. The sensor node consists of a patch antenna-sensor and a UWB Tx/Rx antenna connected with a microstrip transmission line. The Tx/Rx antenna is used

to receive the wide band interrogation signal from the interrogator and re-broadcast the signals reflected by the antenna sensor (i.e. the antenna sensor backscattering) back to the wireless interrogator. To avoid the self-jamming problem [16], the microstrip transmission line is used to introduce a time delay between the background clutter, including the Tx/Rx antenna backscattering, and the antenna sensor backscattering. As long as the transmission line is of sufficient length, the antenna reflection can be distinguished from the background clutter in the time domain.

The wireless interrogator is based on measuring the two-port transmission scattering parameter, i.e. the S21 parameter, between the two interrogation antennas. A linear chirp interrogation signal was generated and broadcasted to the passive wireless sensor through the interrogation antenna connected to port 1 of the interrogator. This interrogation signal is received by the UWB Tx/Rx antenna of the sensor node and transmitted to the antenna-sensor via the microstrip delay line. Upon reaching the antenna-sensor, the portion of the interrogation signal that matches the antenna resonant frequency is received and radiated by the antenna-sensor. The remaining interrogation signal is reflected by the antenna sensor and broadcasted back to the interrogator via the Tx/Rx antenna. As such, the reflection coefficient of the antenna-sensor is encoded into the backscattered signal. The power of the antenna backscattering received by the interrogator can be calculated using Friis equation as

$$P_r = P_t G_{it} G_{ir} G_s^2 \left(\frac{\lambda}{4\pi d}\right)^4 S_{11} L_d, \tag{7}$$

where P_t is the power of the transmitted interrogation signal; d is the distance between the wireless interrogator and the Tx/Rx antenna; G_{it} and G_{ir} are the radiation gains of the interrogator Tx/Rx antennas; G_s is the radiation gain of the UWB sensor antenna; λ is the wavelength of the interrogation signal; S_{11} is the reflection coefficient of the antenna-sensor and L_d is the loss introduced by the delay line. The minimum detectable power of the wireless interrogator can be expressed as [11]:

$$P_{r\,\min} = E \cdot B \cdot F \cdot SNR, \tag{8}$$

where E is the thermal energy; $B$is the bandwidth of the receiver; $F$is the noise figure of the interrogator receiver and SNR is the required signal to noise ratio for this system. Substituting (7) into (8), the theoretical maximum interrogation distance can be calculated as

$$d_{\max} = \frac{\lambda}{4\pi}\left(\frac{P_t G_{tt} G_{tr} G_r^2 S_{11} L_d}{E \cdot B \cdot F \cdot SNR}\right)^{\frac{1}{4}}. \tag{9}$$

Based on equation (9), the maximum interrogation distance is estimated to be 2.25 m assuming a transmitted power of 10 dBm, $E = 4 \times 10^{-21}$ J, $B = 0.8$ GHz, $SNR = 20$ dB, $G_{it} = 12$ dBi, $G_{ir} = 12$ dBi, $G_r = 4$ dBi, $L_d = -1$ dB, $S_{11} = -10$ dB, $F = 1$ dB, and a wavelength of 0.12 m.

Once the interrogator receives the backscattered signals, including the antenna sensor backscattering and the background clutter, it is processed by a digital signal processing (DSP) program to separate the antenna sensor backscattering from the background clutter. Frequency analysis can then be performed on the antenna sensor backscattering to extract the resonant frequency of the antenna sensor.

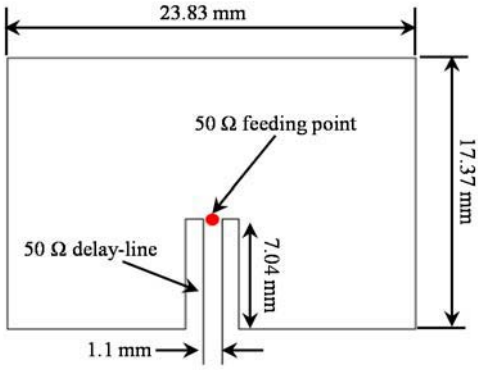

Fig. 2. Physical dimensions and feeding structure of the designed microstrip antenna-sensor.

III. Sensor Node Implementation

A. Design of Temperature Antenna-Sensor

A commercial high frequency circuit laminate, Rogers RO3210 [29], was selected as the substrate material for the wireless sensor because of its high thermal coefficient of dielectric constant α_ε, which is -459 ppm/°C in the temperature range from 0°C to 100°C. Compare to α_ε, its thermal expansion coefficient α_T of 13 ppm/°C is much smaller. Based on equation (6), the theoretical temperature sensitivity of the normalized frequency shift K_T is calculated to be 216.5 ppm/°C. Since RO3210 is a ceramic-filled laminates reinforced with woven fiberglass, its operation temperature is limited by the transition temperature (Tg) of the fiberglass, which is 350°C.

The radiation patch of an antenna-sensor with a designed frequency of 2.45 GHz is shown in Fig. 2. The radiation patch is fed with a 50 Ω microstrip transmission line to excite the fundamental radiation mode along the width direction. In order to obtain a good impedance matching between the transmission line and the radiation patch, the inset fed structure was used. The 50 Ω feeding point was calculated to be at 7.04 mm above the bottom edge of the radiation patch. The length of the transmission line was selected to be 200 mm to ensure sufficient separation between the UWB Tx/Rx antenna and the antenna sensor.

To confirm the antenna design, a three-dimensional (3D) model of the designed antenna-sensor was developed in High Frequency Structure Simulator (HFSS). For a substrate dielectric constant of 10.8 at room temperature (20°C), every 20°C increase in temperature will reduce the dielectric constant by 10.8*459 ppm/°C * 20°C = 0.1. Thus, the substrate dielectric constant of the simulation model was varied from 10.9 to 10.4 with a step of -0.1, which corresponds to temperature changes from 0°C to 100°C. The simulated resonant frequencies were normalized with respect to the frequency at room temperature and are plotted versus the temperature in Fig. 3. The simulated curve displays a high degree of linearity

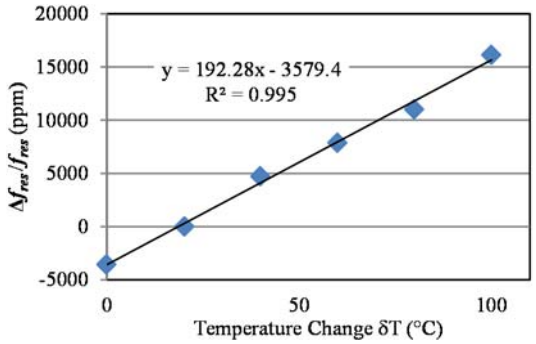

Fig. 3. Simulated relationship between the antenna-sensor's normalized resonant frequency shift and the temperature.

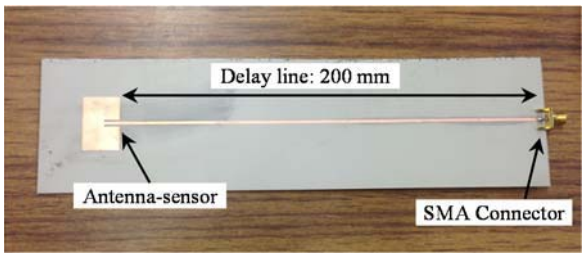

Fig. 4. Fabricated antenna-senor with the microstrip delay line.

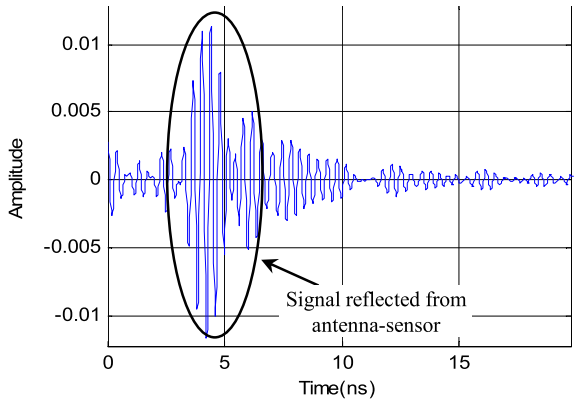

Fig. 5. Time domain signal converted from the measured S11 parameter of the fabricated antenna-sensor with the delay line.

(coefficient of determination $R^2 = 0.995$) and the resulting temperature sensitivity K_T, i.e. the slope of the trend line, is 192.3 ppm/°C, which is slightly lower than the value of 216.5 ppm/°C predicted by the transmission line model.

The antenna-sensor and the delay line were fabricated using a chemical etching technique, as shown in Fig. 4. In order to characterize the round-trip time delay caused by the delay line, a 50 Ω Subminiature version A (SMA) connector was soldered on the end of delay line. The S11 parameter of the fabricated antenna-sensor was firstly measured using a Vector Network Analyzer (VNA) and then converted to the time domain response represented in Fig. 5. The wave packet corresponding to the antenna backscattering starts at 3.5 ns, which is the round-trip time delay between the SMA connector and the antenna-sensor.

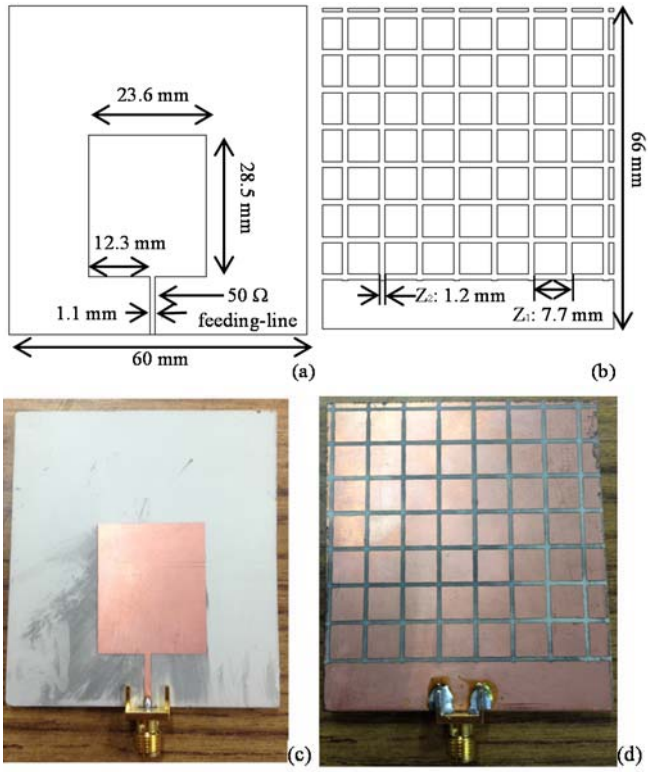

Fig. 6. UWB Tx/Rx antenna: (a) dimensions of the radiation patch; (b) dimensions of the ground plane; (c) top view of the fabricated antenna; and (d) bottom view of the fabricated antenna.

B. Design of UWB Tx/Rx Microstrip Antenna

To implement the entire sensor node on printed circuit boards, the UWB Tx/Rx antenna was developed based on a one-layer substrate patch antenna. The radiation patch is a conventional rectangular patch fed at the bottom edge using a 50 Ω microstrip transmission line, as shown in Fig. 6(a). The ground plane, on the other hand, has a grid pattern with periodically crossed gaps that divide the metallic ground into small square patches (see Fig. 6(b)). The patterned ground plane and the rectangular radiation patch can be considered as a type of metamaterial, namely a RIS structure that acts like a parallel LC resonant circuit [27]. The resonant frequency f_{RIS} of the LC circuit can be determined when it has the largest impedance. The impedance of the LC circuit can be expressed by the impedance of the equivalent inductor X_L and capacitor X_C, i.e.

$$Z_{LC} = j\frac{X_L X_C}{X_C - X_L}, \tag{10}$$

where X_L and X_C can be calculated as

$$X_L = Z_d \tan(kd) \tag{11}$$

and

$$X_c = \frac{K\,(Z_1/Z_2)}{2\pi f \varepsilon \times \sqrt{1-(Z_1/Z_2)^2} \times (Z_2 - Z_1)}. \tag{12}$$

In which, Z_d and k are the wave impedance and the propagation constant of the substrate material, respectively; d is the substrate thickness; Z_1 andZ_2, as shown in Fig. 6(b),

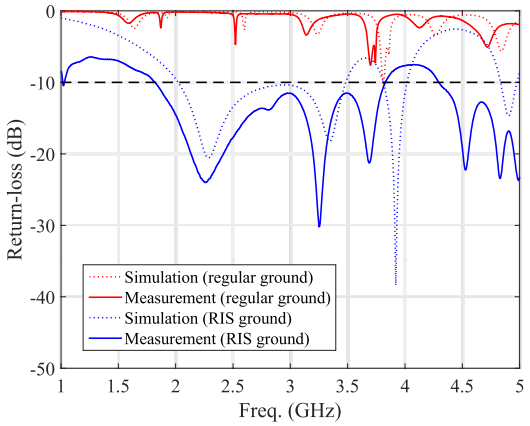

Fig. 7. Comparison between the simulated and measured S11 parameter of the UWB Tx/Rx antenna.

define the vertical coordinates of the strip edges; the function $K()$ is a complete elliptic integral which is defined in [26]. The RIS structure is inductive at frequencies below f_{RIS} while the radiation patch becomes capacitive below its resonant frequency f_{patch}. Therefore, by setting f_{RIS} higher than f_{patch}, the magnetic energy stored in the RIS structure can compensate for the electrical energy stored in the near field of the patch antenna, which results in additional resonances at lower frequencies and thus broaden the bandwidth of the antenna [27].

The design of the UWB Tx/Rx antenna started with a conventional patch antenna having a perfect ground plane. The resonant frequency of the conventional patch antenna f_{patch} was chosen to be at 3.8 GHz and the resonant frequency of the RIS structure f_{RIS} was selected as 4.2 GHz, which is slightly higher than f_{patch}. Base on the properties of the substrate material and the selected f_{RIS}, the dimensions of the patterned ground, i.e. Z_1 and Z_2, can be calculated to be 1.2 mm and 7.7 mm, respectively, using equation (10), (11) and (12).

The pictures of the radiation patch and the patterned ground plane of the UWB Tx/Rx antenna, fabricated using the chemical etching technique, are shown in Fig. 6(c) and 6(d). The S11 parameter of the fabricated antenna was measured and compared with the simulation results in Fig. 7. The bandwidth of the UWB Tx/Rx antenna, determined at the -10 reflection coefficient, is 1.6 GHz (i.e. from 1.9 to 3.5 GHz), which matches with the simulation very well. Compare to the conventional patch antenna, the -10 dB operation bandwidth of the metamaterial antenna increases by more than 100 times. The gain of the Tx/Rx antenna, measured using a two-port transmission test, is shown in Fig. 8. The antenna displayed a relatively flat gain, varying from 3.3 to 4 dBi in frequencies ranging from 2.2 GHz to 3 GHz. Due to its flat gain and wide bandwidth, the temperature sensitivity of the Tx/Rx antenna will have very little effect on the measurement of the antenna sensor resonant frequency.

After validating the performances of the antenna sensor and the Tx/Rx antenna separately using SMA connectors, both antennas were integrated on one RO3210 laminate by connecting them using a 200 mm microstrip transmission line. The entire sensor node was fabricated using chemical etching

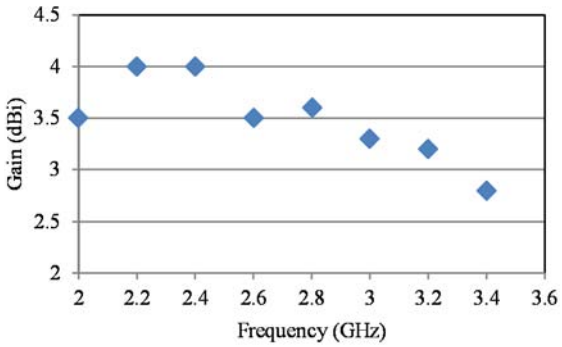

Fig. 8. Measured radiation gain of the fabricated UWB Tx/Rx antenna.

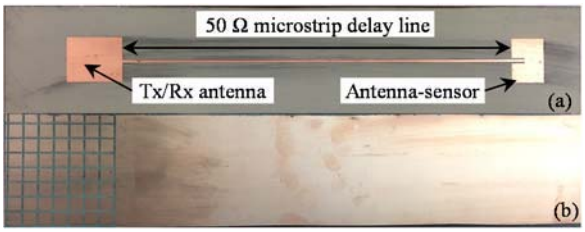

Fig. 9. Fabricated wireless temperature sensor node: (a) top view and (b) bottom view.

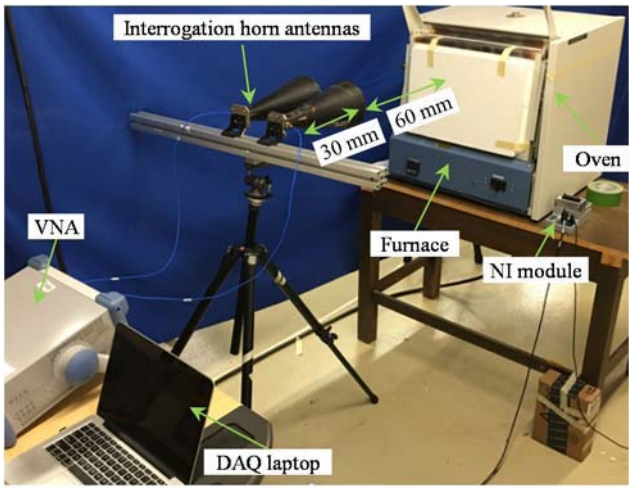

Fig. 10. Experimental setup for thermal testing.

and the pictures of its front and back surfaces are shown in Fig. 9.

IV. Instrumentation and Experimental Setup

A. Hardware Setup

The experimental setup for validating the temperature sensing capability of the antenna sensor as well as its wireless interrogation is shown in Fig. 10. The sensor node was placed inside an oven so that the environment temperature can be precisely controlled. For wireless interrogation, the metal panel of the oven door was removed but the insulation element was kept in place to prevent heat convection so that a stable temperature can be maintained inside the oven. The insulation element of the oven is made of a high temperature material that has a dielectric constant similar to air. Therefore, the insulation material will not introduce any additional changes on the phase or amplitude of the interrogation signal. The wireless

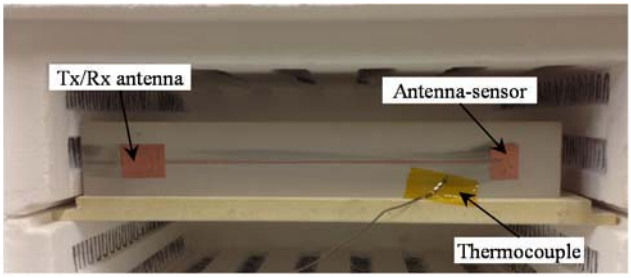

Fig. 11. Wireless sensor node placed at the entrance of the oven.

interrogator was realized by using a VNA and two horn antennas. The horn antennas were placed at an interrogation distance of 60 cm in front of the temperature oven facing the Tx/Rx antenna. These two horn antennas were connected to a two-port VNA using co-axial cables so that the transmitting S-parameter, i.e. the S21 parameter, can be acquired. The VNA was calibrated up to the feeding points of the interrogation antennas, which was 30 cm from the aperture of the interrogation antenna. Therefore, the wireless transmission distance between the feeding points of the integration antennas and the sensor node was 90 cm.

The sensor node was placed near the entrance of the temperature oven, as shown in Fig. 11. A T-type thermocouple was installed adjacent to the antenna-sensor to obtain the reference temperature. The thermocouple measurements were acquired using a National Instruments (NI) thermocouple module. Both the NI thermocouple module and the VNA were connected to a laptop; the communication between the laptop and the VNA was achieved via a wired local-area-network (LAN) connection while the communication between the computer and the NI module was achieved via a Universal Serial Bus (USB) connection. A LabVIEW program was developed to control the VNA and the NI module. The VNA was programmed to acquire the S21 parameters with a frequency resolution of 200 kHz over a frequency range of 2.2 to 3 GHz. The interrogation power was set to be 10 dBm. The S21 parameters were recorded every 2.3 seconds. At the meantime, the thermocouple readings were recorded every 0.1 second. Both recorded data were time stamped for easily correlation between the thermocouple readings and the resonant frequency extracted from the S21 parameters.

V. Digital Signal Processing

A DSP algorithm was developed to extract the resonant frequency of the antenna-sensor from the measured S21 parameters. The flow chart of the DSP algorithm is shown in Fig. 12(a) and the signals corresponding to each block are shown sequentially in Fig. 12(b). First, the acquired S21 parameter, which has a frequency range from f_1 to f_2, is zero padded from the direct current (DC) frequency (i.e. 0 Hz) to f_1. The zero-padded S parameter is then converted to a time-domain signal using Inverse Fast Fourier Transform (IFFT) [30]. As shown in Fig. 12(b), the resulting time-domain signal displays two major wave packets that correspond to the structural backscattering and the antenna sensor backscattering. Both wave packets have small side lobes, which can be reduced by windowing before the IFFT.

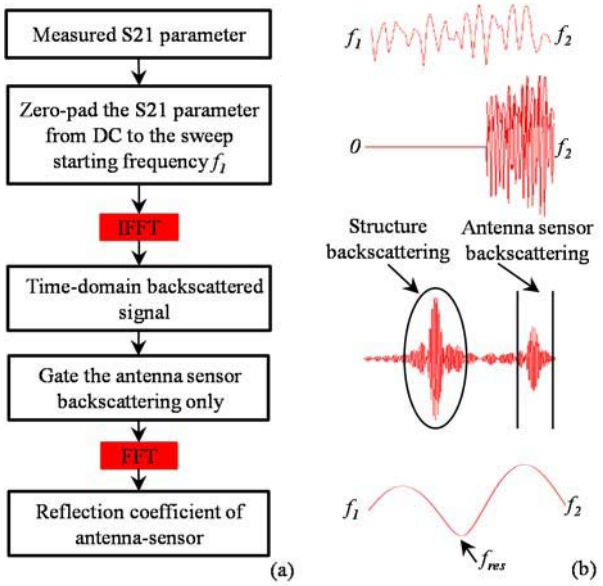

Fig. 12. Digital signal processing algorithm: (a) flow diagram and (b) signals corresponding to processing blocks.

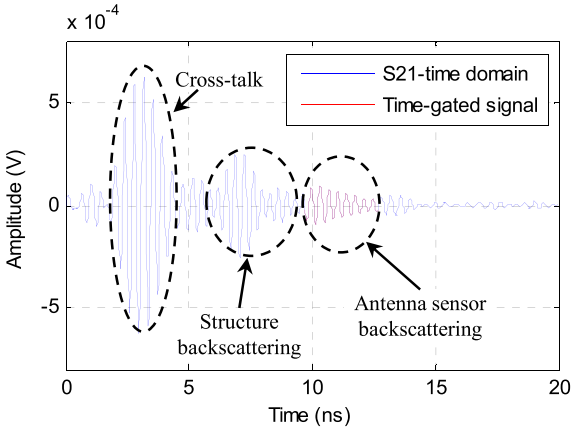

Fig. 13. Time-domain backscattered signal converted from the measured S21 parameter.

Nonetheless, the presents of the side lobes will not have an effect on determining the frequency of the antenna sensor backscattering. Even though the signals backscattered by the Tx/Rx antenna and the surrounding structures usually have the largest amplitude, they appear at a different time span from that of the antenna sensor backscattering. Therefore, a gating window can be applied to the time domain signal to extract the antenna sensor signal. Since the time-gated signal will only contain signals that are reflected at or near the feeding point of the antenna sensor, the time gating process also eliminate reflections at other locations along the transmission delay line due to temperature gradient, etc. Subsequently, the gated signal is converted back to the frequency domain using Fast Fourier Transform (FFT) and the resonant frequency of the antenna-sensor can be determined as the frequency at which the reflection coefficient has the lowest value.

VI. Results and Discussions

The time-domain representation of a typical S21 parameter is shown in Fig. 13. Time "0" corresponds to the feeding point

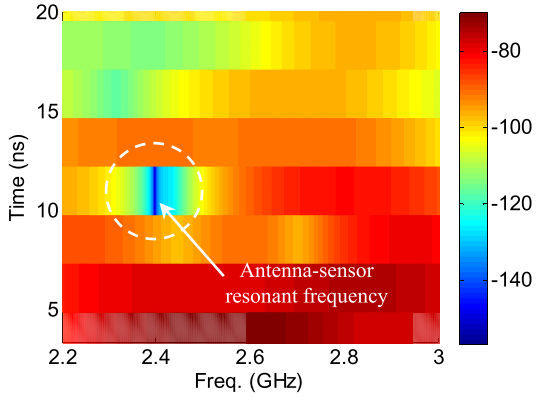

Fig. 14. Spectrogram of the backscattered signal.

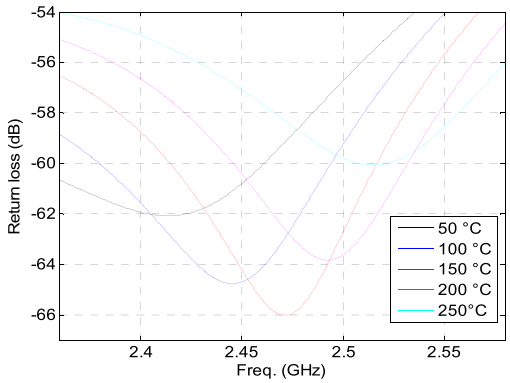

Fig. 15. Spectra of the gated time-domain signals at different temperatures.

of the transmitting interrogation horn antenna. The first wave packet arrives at around 2 ns, which corresponding to a round trip distance of 0.3 m in air. This distance coincides with the distance between the feeding point of the interrogation antenna and the antenna aperture. Therefore, we can conclude that this wave packet is due to the cross-talk between the two interrogation horn antennas. The second wave package arrives at around 6 ns, which corresponds to a round-trip distance of 0.9 m in air and thus is the structure mode backscattering generated by the Tx/Rx antenna and the temperature oven. The antenna sensor backscattering occurs at around 9.5 ns. The time difference between the structure mode and the antenna sensor mode is therefore around 3.5 ns, which matches with the delay time introduced by the transmission line very well. In addition, we can also determine the antenna sensor backscattering from the spectrogram of the backscattered signal. The signal backscattered by the antenna sensor should have a low amplitude at its resonant frequency while the structure mode backscattering usually have frequency components over the entire interrogation bandwidth. As shown in Fig. 14, the spectrogram of the backscattered signal, calculated using Short Time Fourier Transform (STFT), has a low energy band at around 2.4 GHz starting from 9.5 ns to 12.5 ns, which is the designed antenna resonant frequency. At other time windows, the energy are spread over large frequency spans. Therefore, we can easily determine that the starting and stopping time of the time gating window should be at 9.5 ns and 12.5 ns. The frequency spectra of the time gated signal at different temperatures are shown in Fig. 15. The resonant frequency

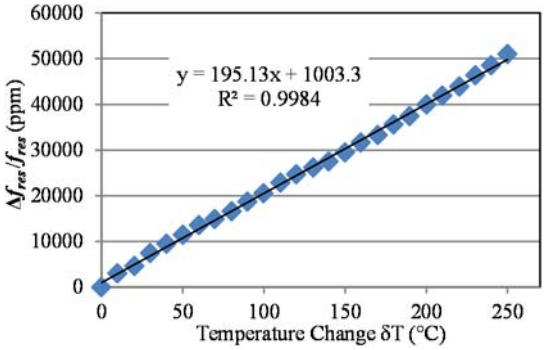

Fig. 16. Measured relationship between the antenna-sensor's normalized resonant frequency shift and the temperature change.

of the antenna sensor is determined as the frequencies at which the frequency spectrum has the lowest amplitude. The frequency shifts at different temperatures were normalized with respect to the resonant frequency of the antenna-sensor at room temperature. The measured normalized frequency shifts are plotted versus the temperature change measured from the thermocouple in Figure 16. The measurement data display a high degree of linearity ($R^2 = 0.9972$). The slope of the trend line is 195.13 ppm/°C, which is slightly higher than the simulated K_T value of 192.45 ppm/°C. The normalized deviation between the simulated and experimental K_T is 1.39%.

VII. Conclusion

In this paper, a wireless temperature sensor consisting of only microstrip circuit elements and has no other electronic components is demonstrated. A wireless interrogation system that is capable of acquire the sensing signal in the far field of the wireless antenna sensor was developed. Temperature testing up to 280°C was conducted to validate the functionalities of the wireless sensor and its interrogation system. The measured temperature sensitivity of 195.13 ppm/°C matches very well with the theoretical prediction. We selected the patch antenna as the sensing element in this study primarily because of its unique advantages, such as easy of fabrication, multi-sensing modality, etc. However, the presented technique can be applied to any other temperature sensitive microwave resonators as well. In the future, an alternative wireless interrogator will be investigated to reduce the interrogator cost and to increase the interrogation speed. In addition, a commercial PCB substrate was selected in this study for the proof-of-concept purpose. We are currently exploring customized high-temperature PCB material to increase the operation temperature of the wireless antenna sensor.

Disclaimer

not infringe privately owned rights. Reference herein to any specific commercial product, process, or service by trade name, trademark, manufacturer, or otherwise does not necessarily constitute or imply its endorsement, recommendation, or favoring by the United States Government or any agency thereof. The views and opinions of authors expressed herein do not necessarily state or reflect those of the United States Government or any agency thereof.

REFERENCES

[1] P. R. N. Childs, J. R. Greenwood, and C. A. Long, "Review of temperature measurement," *Rev. Sci. Instrum.*, vol. 71, no. 8, pp. 2959–2978 2000.

[2] B. Lee, "Review of the present status of optical fiber sensors," *Opt. Fiber Technol.*, vol. 9, no. 2, pp. 57–79, 2003.

[3] Q. Tan *et al.*, "Antenna-resonator integrated wireless passive temperature sensor based on low-temperature co-fired ceramic for harsh environment," *Sens. Actuators A, Phys.*, vol. 236, pp. 299–308, Dec. 2015.

[4] F. Sivrikaya and B. Yener, "Time synchronization in sensor networks: A survey," *IEEE Netw.*, vol. 18, no. 4, pp. 45–50, Jul./Aug. 2004.

[5] I. F. Akyildiz, W. Su, Y. Sankarasubramaniam, and E. Cayirci, "A survey on sensor networks," *IEEE Commun. Mag.*, vol. 40, no. 8, pp. 102–114, Aug. 2002.

[6] J. Yick, B. Mukherjee, and D. Ghosal, "Wireless sensor network survey," *Comput. Netw.*, vol. 52, no. 12, pp. 2292–2330, Aug. 2008.

[7] A. P. Sample, D. J. Yeager, P. S. Powledge, A. V. Mamishev, and J. R. Smith, "Design of an RFID-based battery-free programmable sensing platform," *IEEE Trans. Instrum. Meas.*, vol. 57, no. 11, pp. 2608–2615, Nov. 2008.

[8] F. Kocer and M. P. Flynn, "An RF-powered, wireless CMOS temperature sensor," *IEEE Sensors J.*, vol. 6, no. 3, pp. 557–564, Jun. 2006.

[9] L. M. Reindl and I. M. Shrena, "Wireless measurement of temperature using surface acoustic waves sensors," *IEEE Trans. Ultrason., Ferroelectr., Freq. Control*, vol. 51, no. 11, pp. 1457–1463, Nov. 2004.

[10] D. Girbau, A. Ramos, A. Lazaro, S. Rima, and R. Villarino, "Passive wireless temperature sensor based on time-coded UWB chipless RFID tags," *IEEE Trans. Microw. Theory Techn.*, vol. 60, no. 11, pp. 3623–3632, Nov. 2012.

[11] D. J. Thomson, D. Card, and G. E. Bridges, "RF cavity passive wireless sensors with time-domain gating-based interrogation for SHM of civil structures," *IEEE Sensors J.*, vol. 9, no. 11, pp. 1430–1438, Nov. 2009.

[12] J.-M. Boccard, T. Aftab, J. Hoppe, A. Yousaf, R. Hütter, and L. M. Reindl, "High-resolution, far-field, and passive temperature sensing up to 700 °C using an isolated ZST microwave dielectric resonator," *IEEE Sensors J.*, vol. 16, no. 3, pp. 715–722, Feb. 2016.

[13] H. Cheng, S. Ebadi, and X. Gong, "A low-profile wireless passive temperature sensor using resonator/antenna integration up to 1000 °C," *IEEE Antennas Wireless Propag. Lett.*, vol. 11, pp. 369–372, Apr. 2012.

[14] H. Kairm *et al.*, "Concept and model of a metamaterial-based passive wireless temperature sensor for harsh environment applications," *IEEE Sensors J.*, vol. 15, no. 3, pp. 1445–1452, Mar. 2015.

[15] Q. Tan *et al.*, "Wireless passive temperature sensor realized on multilayer HTCC tapes for harsh environment," *J. Sensors*, vol. 2015, Oct. 2015, Art. no. 124058.

[16] H. Huang, "Flexible wireless antenna sensor: A review," *IEEE Sensors J.*, vol. 13, no. 10, pp. 3865–3872, Oct. 2013.

[17] A. Deivasigamani, A. Daliri, C. H. Wang, and S. John, "A review of passive wireless sensors for structural health monitoring," *Mod. Appl. Sci.*, vol. 7, no. 2, pp. 57–76, 2013.

[18] S. Deshmukh and H. Huang, "Wireless interrogation of passive antenna sensors," *Meas. Sci. Technol.*, vol. 21, no. 3, p. 035201, 2010.

[19] X. Yi, T. Wu, Y. Wang, R. T. Leon, M. M. Tentzeris, and G. Lantz, "Passive wireless smart-skin sensor using RFID-based folded patch antennas," *Int. J. Smart Nano Mater.*, vol. 2, no. 1, pp. 22–38, 2011.

[20] Q. Qiao, L. Zhang, F. Yang, Z. Yue, and A. Z. Elsherbeni, "Reconfigurable sensing antenna with novel HDPE-BST material for temperature monitoring," *IEEE Antennas Wireless Propag. Lett.*, vol. 12, pp. 1420–1423, 2013.

[21] M. Hasani, A. Vena, L. Sydanheimo, L. Ukkonen, and M. M. Tentzeris, "Implementation of a dual-interrogation-mode embroidered RFID-enabled strain sensor," *IEEE Antennas Wireless Propag. Lett.*, vol. 12, pp. 1272–1275, 2013.

[22] J. Yao, S. Tjuatja, and H. Huang, "Real-time vibratory strain sensing using passive wireless antenna sensor," *IEEE Sensors J.*, vol. 15, no. 8, pp. 4338–4345, Aug. 2015.

[23] H. Cheng, S. Ebadi, X. Ren, and X. Gong, "Wireless passive high-temperature sensor based on multifunctional reflective patch antenna up to 1050 degrees centigrade," *Sens. Actuators A, Phys.*, vol. 222, pp. 204–211, Feb. 2015.

[24] A. Daliri, A. Galehdar, W. S. T. Rowe, S. John, C. H. Wang, and K. Ghorbani, "Quality factor effect on the wireless range of microstrip patch antenna strain sensors," *Sensors*, vol. 14, no. 1, pp. 595–605, 2014.

[25] J. W. Sanders, J. Yao, and H. Huang, "Microstrip patch antenna temperature sensor," *IEEE Sensors J.*, vol. 15, no. 9, pp. 5312–5319, Sep. 2015.

[26] H. Mosallaei and K. Sarabandi, "Antenna miniaturization and bandwidth enhancement using a reactive impedance substrate," *IEEE Trans. Antennas Propag.*, vol. 52, no. 9, pp. 2403–2414, Sep. 2004.

[27] L.-W. Li, Y.-N. Li, T. S. Yeo, J. R. Mosig, and O. J. Martin, "A broadband and high-gain metamaterial microstrip antenna," *Appl. Phys. Lett.*, vol. 96, no. 16, p. 164101, 2010.

[28] C. Balanis, *Antenna Theory: Analysis and Design*, 3rd ed. New York, NY, USA: Wiley, 2005.

[29] *RO3000 Series Circuit Materials Datasheet*, Rogers Corp., Rogers, CT, USA, 2011.

[30] H. Huang and T. Bednorz, "Introducing S-parameters for ultrasound-based structural health monitoring," *IEEE Trans. Ultrason., Ferroelectr., Freq. Control*, vol. 61, no. 11, pp. 1856–1863, Nov. 2014.

Jun Yao was born in Jiangsu, China, in 1986. He received the M.S. degree in electrical engineering from the University of Shanghai for Science and Technology, Shanghai, China, in 2012. He is currently pursuing the Ph.D. degree with the Department of Electrical Engineering, University of Texas at Arlington. His research interests include wireless sensor technology for structural health monitoring, IC circuit design for RF energy harvester and antenna interrogation, and digital signal processing.

Franck Mbanya Tchafa received the M.Eng. (Hons.) degree in aerospace engineering from the City University of London, London, U.K., in 2010. He is currently pursuing the Ph.D. degree with the Department of Mechanical and Aerospace Engineering, University of Texas at Arlington. His research interests cover wireless sensor technology and the design and analysis of distributed antenna sensors for structural health monitoring.

Ankur Jain received the B.Tech. degree from the Indian Institute of Technology, Delhi, in 2001, and the M.S. and Ph.D. degrees from Stanford University, in 2003 and 2007, respectively, all in mechanical engineering. He is currently an Assistant Professor of Mechanical and Aerospace Engineering with the Microscale Thermophysics Laboratory, University of Texas at Arlington, where he is the Director of Mechanical and Aerospace Engineering. His research interests include thermal measurements, energy conversion and sustainability, heat transfer, and electrochemistry. He is a recipient of the NSF CAREER Award (2016) and the ASME Electronics and Photonics Packaging Division Young Engineer of the Year Award (2013).

Saibun Tjuatja (SM'03) received the B.S.E.E. degree from the University of Texas at Arlington (UTA), the M.S.E.E. degree from Purdue University, and the Ph.D. degree in electrical engineering from UTA. He is currently an Associate Professor and Director of the Wave Scattering Research Center, Department of Electrical Engineering, UTA, where he has been a Faculty Member since 1993. His current research interests include wave propagation and scattering in random media, remote sensing and radar imaging, subsurface sensing, and wireless structural health monitoring. He is a member of Tau Beta Pi and Sigma Chi, and a Fellow of the Electromagnetic Academy.

Haiying Huang (M'98) received the B.Eng. degree in aircraft propulsion from the Beijing University of Aeronautics and Astronautics in 1987, the M.S. degree in electrical engineering and the Ph.D. degree in aerospace engineering from the Georgia Institute of Technology, in 1997 and 1998, respectively. She is a Professor of Mechanical and Aerospace Engineering with the University of Texas at Arlington. Her current research interests are focused on developing wireless, microwave, ultrasonic, and optical fiber sensors for structural health monitoring. She is a recipient of the NSF CAREER Award (2009).

PAPER

Microstrip patch antenna for simultaneous strain and temperature sensing

IOP Publishing Smart Materials and Structures
Smart Mater. Struct. 27 (2018) 065019 (10pp) https://doi.org/10.1088/1361-665X/aabd47

Microstrip patch antenna for simultaneous strain and temperature sensing

F Mbanya Tchafa and H Huang

Department of Mechanical and Aerospace Engineering, University of Texas at Arlington, 500 W. First Street, WH211, Arlington, TX 76010, United States of America

E-mail: huang@uta.edu

Received 15 September 2017, revised 28 March 2018
Accepted for publication 11 April 2018
Published 8 May 2018

Abstract

A patch antenna, consisting of a radiation patch, a dielectric substrate, and a ground plane, resonates at distinct fundamental frequencies that depend on the substrate dielectric constant and the dimensions of the radiation patch. Since these parameters change with the applied strain and temperature, this study investigates simultaneous strain and temperature sensing using a single antenna that has two fundamental resonant frequencies. The theoretical relationship between the antenna resonant frequency shifts, the temperature, and the applied strain was first established to guide the selection of the dielectric substrate, based on which an antenna sensor with a rectangular radiation patch was designed and fabricated. A tensile test specimen instrumented with the antenna sensor was subjected to thermo-mechanical tests. Experiment results validated the theoretical predictions that the normalized antenna resonant frequency shifts are linearly proportional to the applied strain and temperature changes. An inverse method was developed to determine the strain and temperature changes from the normalized antenna resonant frequency shifts, yielding measurement uncertainty of 0.4 °C and 17.22 $\mu\varepsilon$ for temperature and strain measurement, respectively.

Keywords: antenna sensor, temperature-compensated, strain sensor, temperature sensor, structural health monitoring, wireless sensor

(Some figures may appear in colour only in the online journal)

1. Introduction

Patch antennas have been studied not only for wireless communication, but also for structural health monitoring (SHM) [1, 2]. SHM is a vital technology that implements real-time condition monitoring or damage detection mechanisms for safety assurance of structural systems such as aircraft, power stations, bridges, dams, buildings, large machinery, etc [3]. Without proper and timely maintenance, mechanical systems are prone to structural failures since they experience several detrimental factors such as harsh environments, excessive loads, vibrations, fatigue, etc. Monitoring strain is essential for tracking these factors and for providing early warning to prevent structural failures.

A review of various strain sensing mechanisms is presented in [4]. The most commonly used strain sensors are the piezoresistive thin film strain gauges [5]. Strain is measured from the minute change in the resistance of the thin film strain gauge using a Wheatstone bridge circuit as a signal conditioner. Since the resistance of a strain gauge is also sensitive to temperature, a reference gauge is usually placed adjacent to the strain gauge to provide temperature reference so that the thermal contribution to the resistance change can be removed from the strain measurements [6]. Although thin film strain gauges have a long history of effective use, measurement errors are still possible due to slight differences in the length and even in the tensions of the electric wires connecting the strain gauge output to the Wheatstone bridge [7]. While Wheatstone bridge embodiments that reduce lead wire effects exist, they add complexity in the signal conditioning circuitry and/or need additional lead wires [8]. Due to these reasons, piezoresistive thin film strain gauges are not favorable for SHM applications since a network of distributed sensors is usually required for reliable and comprehensive condition monitoring. The weight penalty and the complexity associated with the wiring of piezoresistive strain gauges render

the realization of large sensor networks unpractical. Optical fibers with inscribed Bragg gratings have been used as strain sensors for many SHM application due to their light weight, compact size, multiplexing capability, and immunity to electromagnetic interference [9–12]. Since most of these optical fiber sensors rely on a single spectral parameter (i.e. the Bragg wavelength) that is sensitive to both strain and temperature, it is difficult to differentiate the effect of temperature and strain on the Bragg wavelength. To solve this problem, Singh *et al* have employed the spectral bandwidth as a measurand in addition to the Bragg wavelength [12]. Even though optical fiber sensors have been implemented in various SHM applications, they do have intrinsic drawbacks such as fragility, limited strain range, expensive interrogation equipment, etc [13].

Wireless sensing is becoming increasingly popular as it eliminates the high maintenance cost typically associated with cable connections [14]. One example of passive wireless sensing is the radio-frequency identification (RFID) technology. A typical RFID system consist of a reader and a tag. Tags can be classified as passive or active based on the working mechanism and power requirements [15–17]. Passive tags are the least complex and cheapest as there is no internal power supply; the circuitry is energized by the electromagnetic (EM) field transmitted by the reader antenna [15]. Passive RFID sensors can be divided into chip-based or chipless RFID sensors based on whether there is an onboard integrated circuit (IC) chip. In recent years, chip-based RFID sensors have been proposed for temperature sensing [18–23] and for strain sensing [24–29] but not for simultaneous measurements of both parameters. Bhattacharyya *et al* measured the changes in temperature by monitoring the power backscattered by the tag [19]. Sample e*t al* developed a wireless identification and sensing platform to enable an RFID tag to interrogate different sensors for sensing temperature, voltage levels, light, etc [20]. Occhiuzzi *et al* employed a meandering line antenna in an RFID tag for strain measurement [30]. The dimensions of the antenna change with the applied strain, which in turn cause a change in the power backscattered by the tag. Therefore, it was possible to measure strain from the backscattered power. Merilampi *et al* proposed a printed RFID antenna to measure strain from changes in power of the backscattered signal [29]. One of the limitations of RFID based wireless sensor is that the size of the RFID tag is quite large because of their low operation frequency. Yi *et al* proposed an antenna folding technique using vias to reduce the dimension of the RFID antenna; the performance of the proposed sensor was validated by tensile testing, and strain was extracted from the measured resonant frequency of the antenna [24]. Further reduction in the size of the RFID antenna was achieved by adding slots to the radiation patch [27]. The slots increase the current path and thus lower the frequency of the antenna. Since the RFID sensor can only measure strain along one direction, Li *et al* proposed a rosette configuration made of three antenna sensors for measuring multi-axial strain fields [28]. Despite these advances, the major drawbacks of RFID sensors, e.g. the large antenna sizes and the slow interrogation speed, still remain. Moreover, RFID sensors can measure either temperature or strain because they are interrogated at one single frequency.

Chipless RFID tags eliminate the IC chip and either use the length of the delay line or multiple resonators for tag identification purpose [31, 32]. Girbau *et al* realized passive temperature sensing based on time-coded chipless RFID tags. It comprised of an ultra-wideband antenna connected to a delay line loaded with a resistive temperature sensor [32]. Preradovic *et al* presented a chipless RFID sensor with an integrated thermistor for temperature sensing [31]. In both cases, variations in temperature will cause a change in the resistance of the sensor. The resulting impedance mis-match between the tag antenna and the sensor in turn changes the backscattered power. Since a sensor element has to be implemented in these chipless RFID tags, they lack the ability to sense more than one parameter. To circumvent these challenges, Karmakar proposed the use of smart materials rather than external resistors [33]. The proposed sensor employs two spatially separated electric-inductive-capacitive resonators for multiple parameters sensing. To differentiate different sensing parameters, the resonators were coated with smart materials that were tailored to measure a specific parameter; one resonator was coated with polyvinyl alcohol for relative humidity sensing while the other resonator was coated with 0.2 mm thick phenanthrene for temperature detection. However, the problem of cross-sensitivity between these two parameters was not address in their work. Moreover, coating the resonators with smart materials increases the thickness and cost of the sensor tag.

Another widely investigated approach for passive wireless sensing is the microstrip patch antenna. Microstrip patch antenna sensors are especially attractive due to their compact size, light weight, ease of manufacturing, and low fabrication cost [34]. Moreover, if the antennas are fabricated on flexible substrates, they can easily conform to nonplanar surfaces [35–37]. Guo *et al* proposed a fabrication procedure for flexible conductive fabric [35]. Based on the realized conductive fabric and waterproof porous film, a flexible antenna was fabricated and evaluated. It was shown that conductive fabric could be used for the fabrication of flexible antennas. The authors work opens doors to flexible antennas for wireless wearable electronics applications. In the past, patch antennas have been studied for temperature sensing [38–42], and strain sensing [43–51]. These published works, however, have only demonstrated single modality sensing of either temperature or strain from one antenna resonant frequency. Since the antenna resonant frequency depends on the patch dimensions as well as the dielectric constant, it can be influenced by both temperature and strain changes [52, 53]. The effects of strain and temperature on the antenna resonant frequency must be decoupled to measure strain and temperature independently. The easiest way to achieve temperature-compensated strain measurement is to add a second reference sensor that is not subjected to strain and thus only responds to temperature changes. However, such an approach is unattractive for SHM applications as it generally results in an increase in cost, size, and weight of the sensor. Some researchers have attempted to minimize the cross-sensitivity

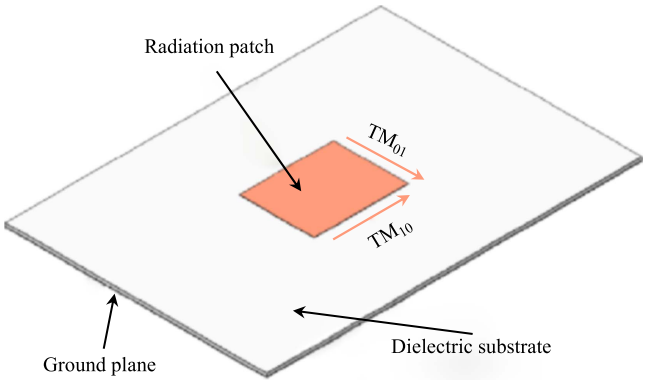

Figure 1. Configuration of a rectangular patch antenna. The radiation patch and the ground plane are made of conductive materials.

between temperature and strain by selecting the thermal coefficient of the substrate dielectric constant accordingly [38, 39, 54]. Solely interested in temperature sensing, Sanders *et al* and Yao *et al* fabricated the antenna sensors on commercial printed circuit board (PCB) with high thermal coefficient of dielectric constant [38, 39]. As such, the temperature sensitivity overwhelmed the strain sensitivity in the frequency response of the antenna sensor. Similarly, Yi *et al* focused on strain measurement only, and selected a commercial PCB with low thermal properties to minimize the problem of cross-sensitivity between temperature and strain [54].

While antenna sensors have been studied for strain and temperature sensing separately, simultaneous measurements of strain and temperature using microstrip patch antenna sensors have not been investigated so far. In this study, we demonstrated a single antenna sensor for simultaneous strain and temperature sensing. To resolve the problem of cross-sensitivity between temperature and strain, we exploit the two fundamental resonant frequencies of a single antenna sensor having a rectangular radiation patch. Based on the transmission line model, the normalized antenna resonant frequency shifts were found to be linearly proportional to the strain and temperature change. By selecting the thermal response of the dielectric substrate material properly, the theoretical prediction was validated by experimental measurements. Curve-fitting the normalized antenna resonant frequency shifts as linear functions of the strain and temperature change enables inversely determining the strain and temperature change from the measured antenna resonant frequency shifts.

2. Principle of operation

A rectangular patch antenna (RPA) is made of a dielectric substrate sandwiched between two conductive layers, i.e. the radiation patch and the ground plane, as shown in figure 1. An RPA possesses two fundamental resonant modes; the TM_{10} mode with current flowing along the length direction and the TM_{01} mode with current flowing along the width direction of the radiation patch. Per the transmission line model, the resonant frequency of the TM_{10} mode, i.e. the f_{10} frequency, can be calculated as

$$f_{10} = \frac{c}{2(L + 2\Delta L)\sqrt{\varepsilon_{re}}}, \tag{1}$$

where c, L, and ε_{re} represent the speed of light, the length of the radiation patch, and the effective dielectric constant respectively [34]. The effective dielectric constant of the antenna ε_{re}, depending on the substrate height h, the width of the radiation patch W, and the dielectric constant of the substrate ε_r, can be expressed as

$$\varepsilon_{re} = \frac{\varepsilon_r + 1}{2} + \frac{\varepsilon_r - 1}{2\sqrt{1+10h/W}}. \tag{2}$$

Because of the finite dimensions of the RPA along the length and width, the radiation fields extend beyond the edges of the radiation patch, forming fringing. As such, the length of the antenna is increased by ΔL, which is a function of ε_{re}, W and h, i.e.

$$\Delta L = 0.412h\frac{(\varepsilon_{re} + 0.3)(W/h + 0.264)}{(\varepsilon_{re} - 0.258)(W/h + 0.813)}. \tag{3}$$

If the height of the substrate is much smaller than the radiation patch dimensions (i.e. $h \ll W$ and $h \ll L$), the effective dielectric constant can be approximated as the dielectric constant of the substrate (i.e. $\varepsilon_{re} \approx \varepsilon_r$). In addition, the line extension ΔL can be neglected. In this case, equation (1) can be reduced to

$$f_{10} = \frac{c}{2L\sqrt{\varepsilon_r}}. \tag{4}$$

The shift of the antenna frequency δf_{10} can be expressed in terms of variations in the patch length L and the substrate dielectric constant ε_r as

$$\delta f_{10} = \frac{\partial f_{10}}{\partial \varepsilon_r}\delta\varepsilon_r + \frac{\partial f_{10}}{\partial L}\delta L. \tag{5}$$

$\partial f_{10}/\partial\varepsilon_r$ and $\partial f_{10}/\partial L$ can be derived from equation (4) as

$$\frac{\partial f_{10}}{\partial \varepsilon_r} = -\frac{1}{2\varepsilon_r}\frac{c}{2L\sqrt{\varepsilon_r}} = -\frac{1}{2\varepsilon_r}f_{10} \tag{6a}$$

and

$$\frac{\partial f_{10}}{\partial L} = -\frac{1}{L}\frac{c}{2L\sqrt{\varepsilon_r}} = -\frac{1}{L}f_{10}. \tag{6b}$$

The normalized frequency shift $\delta f_{10}/f_{10}$ can then be written as

$$\frac{\delta f_{10}}{f_{10}} = -\frac{1}{2}\frac{\delta\varepsilon_r}{\varepsilon_r} - \frac{\delta L}{L}. \tag{7}$$

The first term in the right-hand side of equation (7) represents the normalized dielectric constant change. For sensing purpose, it is important to select a substrate with a normalized dielectric constant change that varies linearly with temperature, i.e.

$$\frac{\delta\varepsilon_r}{\varepsilon_r} = \alpha_{\varepsilon_r}\delta T, \tag{8}$$

where α_{ε_r} is the thermal coefficient of dielectric constant (TCD_k) of the substrate along the length direction [55]. The second term in the right-hand side of equation (7) can be further expanded into two parts: the contribution due to temperature change and the contribution due to applied mechanical strain, i.e.

$$\frac{\delta L}{L} = \frac{\delta L_T}{L} + \frac{\delta L_\varepsilon}{L}, \tag{9}$$

in which $\delta L_\varepsilon/L = \varepsilon_L$ is the applied mechanical strain along the patch antenna length. Representing the coefficient of thermal expansion (CTE) of the radiation patch along the length direction as α_{TL}, we can express $\delta L_T/L$ as

$$\frac{\delta L_T}{L} = \alpha_{TL}\delta T. \tag{10}$$

Substituting equations (8)–(10) in (7) gives

$$\frac{\delta f_{10}}{f_{10}} = -\left(\frac{1}{2}\alpha_{\varepsilon_r} + \alpha_{TL}\right)\delta T - \varepsilon_L. \tag{11}$$

The normalized frequency shift δf_{01} of the TM_{01} mode can be derived following the same process. Assuming the sensor is under uniaxial loading condition and has a Poisson's ratio v, the normalized frequency shift $\delta f_{01}/f_{01}$ can be expressed as

$$\frac{\delta f_{01}}{f_{01}} = -\left(\frac{1}{2}\alpha_{\varepsilon_r} + \alpha_{TW}\right)\delta T + v\varepsilon_L, \tag{12}$$

in which α_{ε_r} and α_{TW} are the TCD_k and the CTE of the substrate along the width direction, respectively.

A general form of equations (11) and (12) can be written as

$$\frac{\delta f_{10}}{f_{10}} = -K_{TL}\delta T - K_{\varepsilon L}\varepsilon_L \tag{13a}$$

and

$$\frac{\delta f_{01}}{f_{01}} = -K_{TW}\delta T + K_{\varepsilon W}\varepsilon_L, \tag{13b}$$

in which $K_{\varepsilon L}$ and $K_{\varepsilon W}$ represent the strain sensitivities along the patch length and width respectively while K_{TL} and K_{TW} represent the temperature sensitivities along the patch length and width respectively.

3. Antenna sensor design and fabrication

3.1. Substrate selection and antenna design

The equations derived above provide the theoretical foundation for selecting the substrate material. Since the purpose is to measure strain and temperature simultaneously, it is important that the temperature sensitivities K_{TL} and K_{TW} do not overwhelm the strain sensitivities $K_{\varepsilon L}$ and $K_{\varepsilon W}$ or vice versa. After researching the properties of commercial substrates, we have selected Rogers RT/duroid 5880 as the substrate material for the antenna sensor. Rogers RT/duroid 5880 is a high frequency polytetrafluoroethylene (PTFE) composite laminate with reinforced glass microfibers. The randomly oriented microfibers result in dielectric constant uniformity. The dielectric constant ε_r of the selected laminate is 2.2 and the TCD_k is -125 ppm °C^{-1}. The CTE values are 31 ppm °C^{-1}, 48 ppm °C^{-1}, and 237 ppm °C^{-1} in x-, y-, and z-direction respectively. Since the TCD_k is larger than the CTE values, the temperature sensitivity of the RPA will be predominantly contributed by the TCD_k. If this substrate is subjected to thermo-mechanical tests without being bonded on any structures, based on its properties and the theoretical expression derived in (11), we predict a K_{TL} value of 31.5 ppm °C^{-1}. Since the strain sensitivity K_L is equal to -1, the thermal contribution to the normalized frequency change due to 1 °C change is equivalent to that of 31.5 $\mu\varepsilon$ in strain. By selecting this substrate, applications are limited to temperatures below 350 °C, which is the glass transition temperature (Tg) of the substrate [56]. The substrate manufacturer recommends using the substrate up to a maximum temperature of 150 °C for thermo-mechanical stability. It is worth mentioning that the maximum operating temperature of the sensor is also limited by the operational temperature of the adhesive used in bonding the sensor to the structural system. The lowest temperature between these two limits determines the maximum operational temperature for the sensor. Therefore, one must select the appropriate adhesive and substrate based on the applications. The substrate thickness was selected to be 0.79 mm. Since we have demonstrated wireless vibration sensing using a substrate with similar thickness [57], and wireless strain sensing using a substrate of 76 μm [44], we are confident the substrate thickness will not be a limiting factor for the wireless capability of the proposed sensor.

The sensor was designed to operate at the fundamental frequencies of approximately f_{10} of 5 GHz and f_{01} of 6 GHz, which gives a length of 15.9 mm and a width of 19.5 mm for the radiation patch. Since an inset-feed would disturb the current fields of the radiation modes, we selected to feed the radiation patch at the edge using a microstrip transmission line, as shown in figure 2. As a result, impedance matching of only one resonant mode, e.g. the TM_{10} mode, can be realized by adjusting the feeding position x_o. The width of the transmission and thus its impedance was selected taking the fabrication limitation and the feeding location into consideration. In our case, we selected the width of the transmission line W_t to be 0.7 mm, leading to an impedance of 100 Ω for the transmission line. In addition, the transmission line also serves as a quarter-wave transformer that matches the impedance of the radiation patch to the 50 Ω SubMiniature version A (SMA) connector. Therefore, its length L_t was calculated to be 11.3 mm at the f_{10} frequency of 5 GHz. Finally, the impedance of the TM_{10} mode was calculated from the impedances of the transmission line and the SMA connector

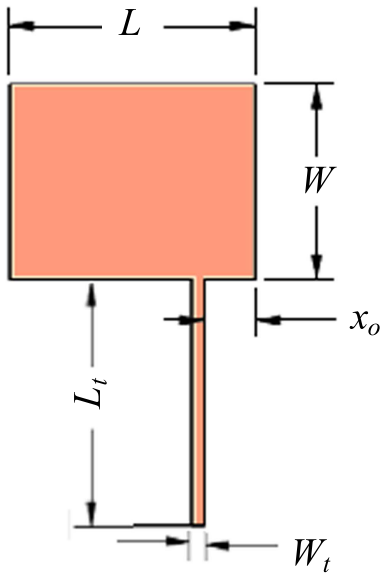

Figure 2. Physical design of the antenna sensor edge fed by a microstrip transmission line.

as 200 Ω, based on which the feeding position x_o was chosen to be 3.8 mm [34].

3.2. Sensor fabrication

The antenna sensor was fabricated by print-etching technique. The sensor pattern was first drawn using a CAD software, and then printed on a PCB transfer paper film (Techniks PNPB20). The printed pattern was then transferred from the film to the selected PCB using a clothing iron as the heat source. Subsequently, the PCB was submerged in ferric chloride for chemical etching to remove the exposed copper surfaces. After chemical etching, the PCB was given a final chemical bath in acetone to remove the ink residues.

The antenna sensor was bonded on a dog-bone specimen using LOCTITE superglue. The dog-bone specimen was made of aluminum 6061-T6 as per ASTM standard E8/E8M—16a. The dog-bone specimen has a thickness, width, and gauge length of 6.5 mm, 40 mm, and 85 mm respectively. The gauge length was chosen as 85 mm to ensure uniaxial loading at the sensor location. To ensure a symmetric configuration of the instrumented specimen, the same substrate used for fabricating the antenna sensor was bonded on the back of the dog-bone specimen. The front and back views of the instrumented specimen are shown in figure 3. Thin film strain gauges (OMEGA SGD5/350 LY13) were bonded on the substrate on the back to measure strain in both transverse and loading directions, as shown in figure 3(b). The pin of the SMA connector was attached to the feed line by soldering. Since the dog-bone specimen also serves as the ground plane to the antenna sensor, the ground of the SMA connector was electrically connected to the dog-bone specimen using conductive epoxy (CircuitWorks CW2400).

To release the specimen from any residual strains due to fabrication, the specimen was subjected to three thermal cycles up to 100 °C at a rate of 2 °C min^{-1}. Once the maximum temperature was achieved, the sample was let to naturally cool to 30 °C. After fabrication and annealing, the resonant frequencies of the antenna sensor were determined by measuring the scattering parameters S_{11} using a vector network analyzer (VNA, Rohde & Schwarz ZVA24). Figure 4 presents a comparison between the simulated and measured S_{11} parameters of the antenna. The simulated results were obtained using High Frequency Structure Simulator. The fabricated antenna does resonate at 5 and 6 GHz as per the design. There is a good agreement between simulation and measurement. The very slight difference between both S_{11} parameters is most likely due to the fabrication and/or the parasitic capacitance introduced by the SMA connector [43]. It is worth noting that the TM_{01} mode displayed a return loss that is below −10 dB, even though the impedance of this radiation mode is not matched to the impedance of the transmission feed line.

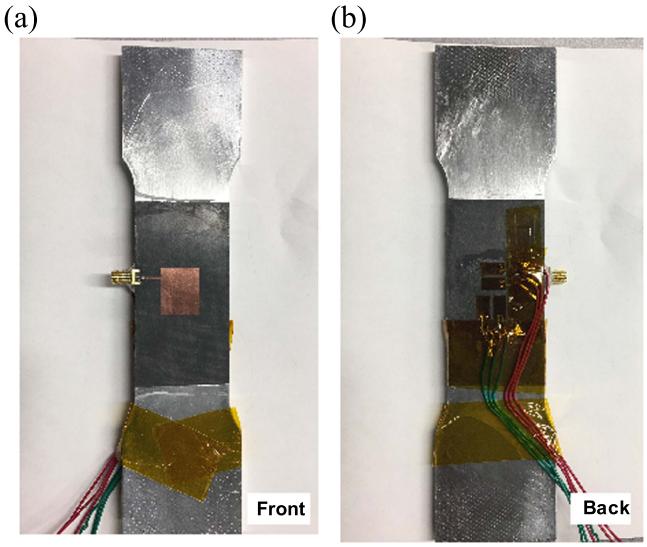

Figure 3. A dog-bone sample instrumented with the antenna sensor; (a) front view; (b) back view.

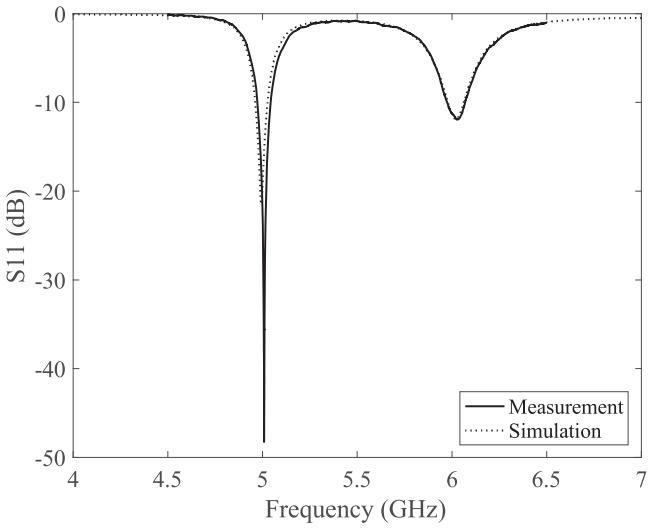

Figure 4. Comparison between simulated and measured S_{11} curves of the antenna sensor.

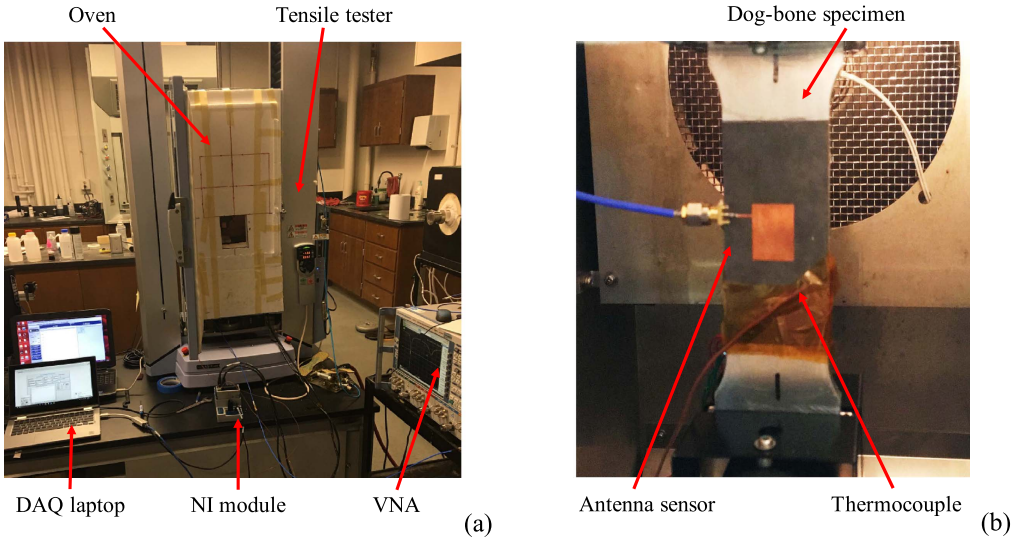

Figure 5. (a) Experimental set up for thermo-mechanical testing of the antenna sensor (b) dog-bone specimen with bonded antenna sensor and thermocouple.

4. Instrumentation and experimental setup

The experimental setup for characterizing the simultaneous effects of temperature and strain on the antenna sensor's frequency response is shown in figure 5(a). A tensile tester (SHIMADZU AG-X plus) equipped with an oven was used to apply the mechanical load and temperature changes on the instrumented specimen. The door of the oven was replaced by a foam box with an opening of 100 mm × 120 mm. When the sample was installed in the tensile tester, the antenna sensor was facing the opening so that no reflection is generated by the foam. The foam panel provides thermal insulation of the specimen while avoiding the reflections usually generated by a metallic oven door. Due to the small opening, hot air will leak from the oven to the surrounding environment. Thus, a thermocouple (OMEGA T-type) was placed near the antenna sensor to measure the sensor temperature, as shown in figure 5(b). Having a manufacturer specified measurement error of 0.5 °C or 0.4% of the measured temperature value (whichever is greater), this thermocouple was selected given its lowest measurement error and cost. To measure the antenna resonant frequency, the antenna sensor was connected to the VNA using a coaxial cable. The VNA was set to sweep 40 000 points between 4.5 and 6.5 GHz, corresponding to a frequency resolution of 50 kHz. By connecting the VNA to a personal computer (PC) using the Ethernet connection, a LabVIEW program running in the PC can be used to acquire and save the S_{11} scattering parameters measured by the VNA along with the measurement data from a strain gauge module (National Instrument, NI 9237) and a thermocouple module (National Instrument, NI 9211).

The instrumented specimen was loaded in increments of 1000 N at a rate of 20 N s^{-1}. Figure 6 presents the strain gauges' measurements during the antenna sensor characterization. Although the strain gauges are self-temperature compensated for aluminum, which has a CTE that differs from the antenna substrate, thermal output from the strain

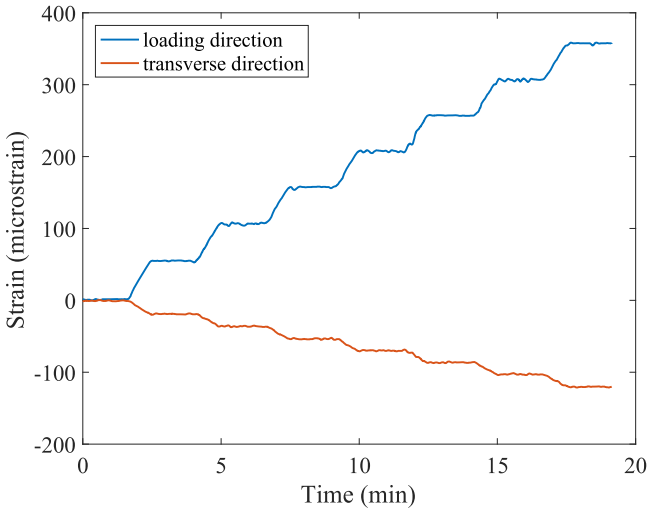

Figure 6. Strain measurements along the loading and transverse directions under different loading levels.

gauges due to the CTE mismatch are not present in the strain measurements. This was achieved by balancing the strain gauge module to zero strain once the desired temperature was achieved and before any load was applied to the specimen. As such, the thermal outputs of the strain gauges were eliminated from the strain gauge' measurements, i.e. the strain measurements are contributed by the mechanical load only. Based on figure 6, 1000 N of load generated strains of 55 $\mu\varepsilon$ and -18.4 $\mu\varepsilon$ along the loading and transverse directions. These values are in good agreement with the theoretical prediction of 54.5 $\mu\varepsilon$ and -18 $\mu\varepsilon$ along these two directions. Dividing the measured sensitivity in the transverse direction to the loading direction gives 0.335—a good agreement with the Poisson's ratio of aluminum 6061-T6 and a confirmation that the instrumented specimen is under uniaxial loading condition. Based on these results, we can draw the conclusion that the strain is transferred to the dielectric substrate faithfully. As shown in figure 6, the specimen was held for a duration of

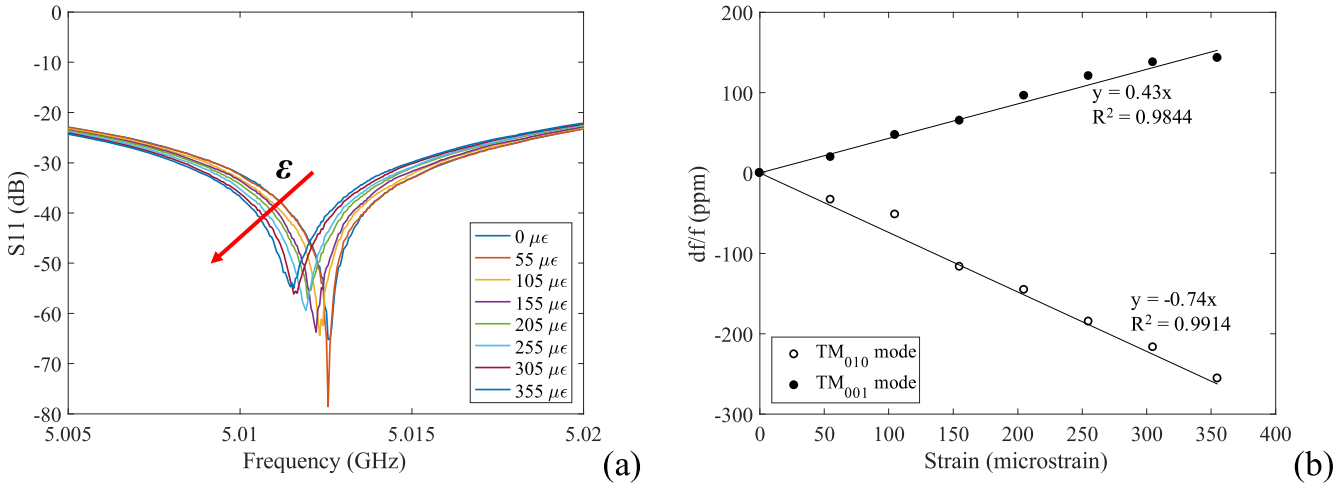

Figure 7. Effect of strain on the resonant frequencies of the patch antenna sensor at 22.4 °C: (a) measured S_{11} parameters of the TM_{10} mode at different strain levels; (b) linear shifts of the normalized antenna frequency with the applied strain.

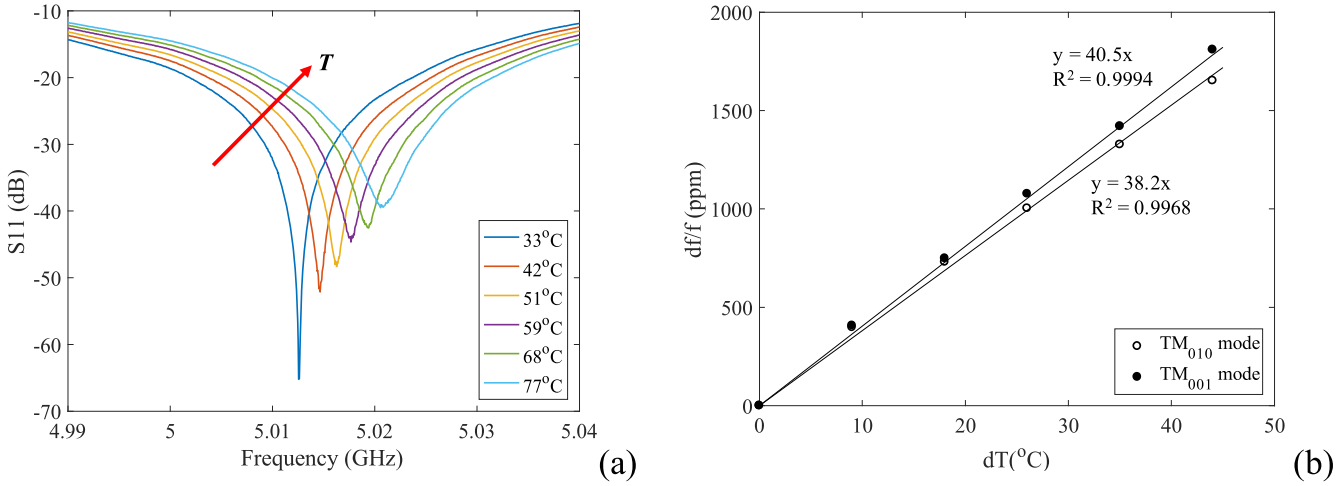

Figure 8. Effect of temperature on the resonant frequencies of the patch antenna sensor: (a) measured S_{11} parameters of the TM_{10} mode at different temperatures; (b) linear shifts of the normalized frequency with the temperature increase.

100 s at each load increment. After each load increase, the specimen was first let to rest for approximately 43 s before taking any measurements from the antenna sensor. All S_{11} curves, temperature, and strain measurements were time stamped for ease of correlation during data analysis.

5. Results and discussions

Before subjecting the antenna sensor to thermo-mechanical tests, the theoretical prediction was first validated by evaluating the sensor's performance due to the applied strain and temperature changes separately. To assess the sensor's performance under strain only, the antenna sensor was subjected to tensile loads along the TM_{10} mode (i.e. along the length of the antenna sensor). With an increase in strain under constant room temperature of 22.4 °C, as derived in (11), the S_{11} curves of the TM_{10} mode are expected to shift to the left. This effect is presented in figure 7(a) where the f_{10} resonant frequency of the antenna sensor decreases with the applied strain. Figure 7(b) presents the normalized resonant frequency shifts of the antenna sensor as a function of applied strain. The measured strain sensitivities were -0.74 ppm/$\mu\varepsilon$ and 0.43 ppm/$\mu\varepsilon$ for the TM_{10} and TM_{01} modes respectively. The data presented in figure 7(b) display excellent linearity given the R^2 values of 0.9914 and 0.9844 for the TM_{10} and TM_{01} modes respectively. The measured strain sensitivities of the f_{10} frequency differ slightly from the theoretical prediction, which predicts a 1:1 ratio between the applied strain and the normalized resonant frequency shift. This difference is probably due to shear lag introduced by the bonding layer [43].

Since the TCD_k of the substrate, Rogers RT/duroid 5880, is negative and much greater in magnitude than the CTE of aluminum, an increase in temperature, under zero load, causes the S_{11} curves of the antenna sensor to shift to the right, as validated by the experiment results shown in figure 8(a). The temperature sensitivity of both the TM_{10} and TM_{01} modes were obtained by plotting the normalized resonant frequency shifts as a function of temperature shown in

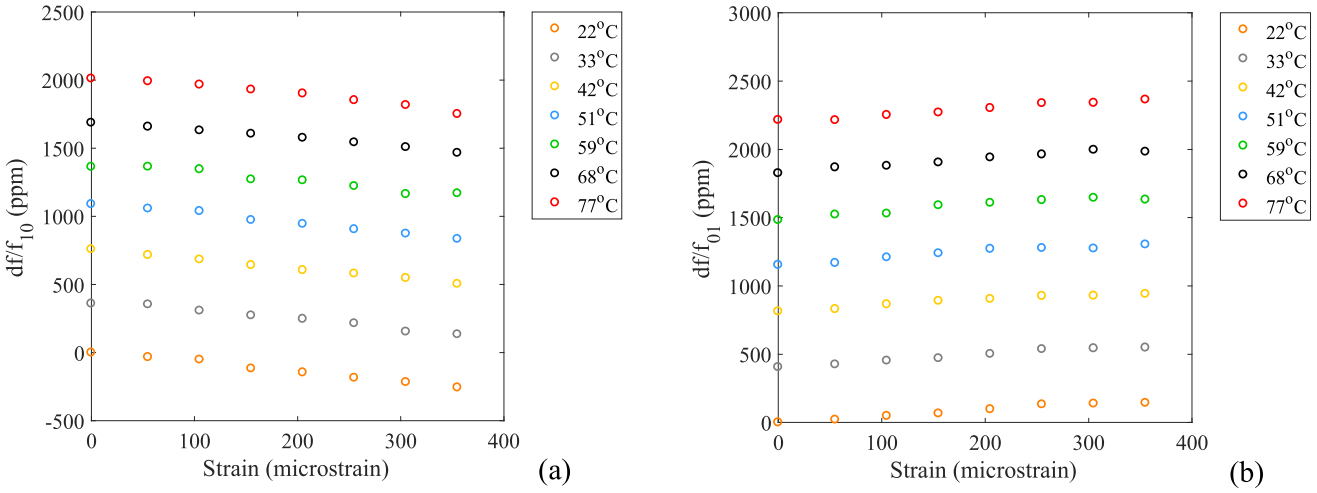

Figure 9. The normalized antenna frequency shifts with the applied strain under different temperatures; (a) TM_{10} mode and (b) TM_{01} mode.

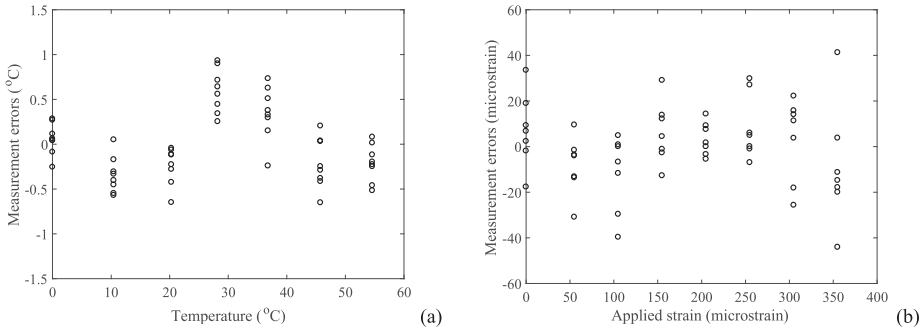

Figure 10. Differences between (a) temperature; and (b) strain inversely determined from the normalized antenna resonant frequency shifts and those measured using a thermocouple and strain gauges respectively.

figure 8(b). The temperature sensitivity of TM_{10} mode was measured as 38.2 ppm °C^{-1} while the temperature sensitivity of the TM_{001} mode was measured as 40.5 ppm °C^{-1}. The data presented in figure 8(b) display excellent linearity judging from the R^2 values of 0.9968 and 0.9994 for the TM_{10} and TM_{01} modes respectively. Given the TCD_k of the substrate and the CTE of aluminum of 23.4 ppm °C^{-1} [58], the theoretical prediction for the temperature sensitivity of the antenna sensor as derived in (13*a*) is 39.1 ppm °C^{-1}. The measured sensitivity of the antenna sensor along the TM_{10} mode is 2.3% smaller than the theoretical prediction while the measured temperature sensitivity along the TM_{001} mode is 3.6% greater than the theoretical prediction—a good agreement between the theory and the measurements.

To establish a direct relationship between the antenna sensor outputs, i.e. the antenna resonant frequency shifts $\delta f_{10}/f_{10}$ and $\delta f_{01}/f_{01}$, and the desired measurands (i.e. the temperature and strain changes), the standard sensor calibration procedure as specified in [8, 59] was followed. The antenna sensor was loaded in increments of 55 $\mu\varepsilon$ up to 355 $\mu\varepsilon$ while being exposed to temperatures from 22 °C to 77 °C. The responses of the antenna resonant frequencies to simultaneous temperature and strain changes are plotted in figure 9. Since the thickness of the dog-bone specimen was chosen as 6.5 mm and its modulus of elasticity is seventy times higher than that of the substrate, the substrate was expected to expand at the same rate as the dog-bone specimen under the applied strain. As expected, the normalized f_{10} frequencies, under constant temperature, decreases with increases in the applied strain since the strain was applied in the TM_{10} mode direction. The opposite effect is shown in figure 9(b), where the normalized f_{01} frequency at a constant temperature increase with the applied strain due to the Poisson's effect. This is in good agreement with the theory derived in (11) and (12). The effect of temperature is noticeable as the normalized resonant frequencies of both modes increase with temperature increase at constant strain values. Both normalized resonant frequencies appear to be linearly proportional to strain, as well as, to temperature. Therefore, they are curve fitted to linear functions using the curve fitting tool in MATLAB, which leads to

$$\frac{\delta f_{10}}{f_{10}} = 37.43\delta T - 0.6861\varepsilon_L \tag{14a}$$

and

$$\frac{\delta f_{01}}{f_{01}} = 40.49\delta T + 0.4302\varepsilon_L, \tag{14b}$$

where δT represents the change in temperature and ε_L is the applied tensile strain. The curve fitting indicated excellent linearity, yielding a R^2 value of 0.9991 for the TM_{10} mode and 0.9995 for the TM_{001} mode. Inverting (14*a*) and (14*b*)

produces the 'calibration curve' of the antenna sensor, i.e.

$$\begin{bmatrix} \varepsilon_L \\ \delta T \end{bmatrix} = \begin{bmatrix} -0.6861 & 37.43 \\ 0.4302 & 40.49 \end{bmatrix}^{-1} \times \begin{bmatrix} \dfrac{\delta f_{10}}{f_{10}} \\ \dfrac{\delta f_{01}}{f_{01}} \end{bmatrix} \begin{pmatrix} \mu\varepsilon \\ ^\circ\mathrm{C} \end{pmatrix}. \quad (15)$$

Plugging any measured antenna frequency shifts into equation (15) produces the corresponding strain and temperature values. To determine the calibration errors, the strain and temperature determined from the measured antenna frequency shifts using equation (15) are compared with the strain and temperature values measured using the strain gauges and the thermocouple. The differences between these two sets of measurements are presented in figure 10. The measurement errors for temperature are within $-0.7\,^\circ$C and $1\,^\circ$C while the measurement errors for strain are within $\pm 40\,\mu\varepsilon$. One standard deviation gives a temperature error of $\pm 0.4\,^\circ$C and a strain error of $\pm 17.22\,\mu\varepsilon$. The temperature error is well within the manufacturer's specified error value of $\pm 0.5\,^\circ$C. These results validate the capability of a single RPA for simultaneous strain and temperature sensing.

6. Conclusion

We demonstrated that a single microstrip patch antenna with a rectangular radiation patch is capable of sensing strain and temperature simultaneously. A theoretical model representing the normalized antenna resonant frequency shift as linear functions of strain and temperature changes was established and validated by experiment measurements. The theoretical model also suggests that the thermal response of the dielectric substrate should be selected properly to achieve a balanced response of the antenna sensor to temperature and strain changes. In the future, we will explore high-temperature substrate materials as well as wireless interrogation of the antenna sensor to increase the maximum operating temperature.

Acknowledgments

The authors would like to thank Mr Mike Braden from Rogers Corporation for providing the high-frequency Printed Circuit Boards used for this research, and Mr Brian Shonkwiler from the University of Texas Arlington for providing the training required to safely operate the tensile tester.

Disclaimer

ORCID iDs

F Mbanya Tchafa https://orcid.org/0000-0003-2527-8343
H Huang https://orcid.org/0000-0003-0484-7615

References

[1] Li L W, Li Y N, Yeo T S, Mosig J R and Martin O J F 2010 A broadband and high-gain metamaterial microstrip antenna *Appl. Phys. Lett.* **96** 164101
[2] Chang F-K 2016 *Structural Health Monitoring 2013, Volume 1 and 2—A Roadmap to Intelligent Structures* (Lancaster, PA: DEStech)
[3] Rao B K N 1996 *Handbook of Condition Monitoring* (Oxford: Elsevier)
[4] Jia Y, Sun K, Agosto F J and Quiñones M T 2006 Design and characterization of a passive wireless strain sensor *Meas. Sci. Technol.* **17** 2869–76
[5] Yao J, Hew Y Y M, Mears A and Huang H 2015 Strain gauge-enable wireless vibration sensor remotely powered by light *IEEE Sens. J.* **15** 5185–92
[6] Vishay Precision Group 2010 Strain gage thermal output and gage factor variation with temperature *Technical Note* TN-504-1 vol 11054 pp 35–47
[7] Baher H 2001 *Analog and Digital Signal Processing* 2nd edn (New York: Wiley)
[8] Bentley J P 2005 *Principles of Measurement Systems* 4th edn (Upper Saddle River, NJ: Prentice Hall)
[9] Chen G, Liu L, Jia H, Yu J, Xu L and Wang W 2004 Simultaneous strain and temperature measurements with fiber bragg grating written in novel Hi-Bi optical fiber *IEEE Photonics Technol. Lett.* **16** 2003–5
[10] Song D *et al* 2014 A simultaneous strain and temperature sensing module based on FBG-in-SMS *Meas. Sci. Technol.* **25** 055205
[11] Singh A K, Zhu Y, Han M and Huang H 2016 Simultaneous load and temperature measurement using Lophine-coated fiber Bragg gratings *Smart Mater. Struct.* **25** 115019
[12] Singh A K, Berggren S, Zhu Y, Han M and Huang H 2017 Simultaneous strain and temperature measurement using a single fiber Bragg grating embedded in a composite laminate *Smart Mater. Struct.* **26** 115019
[13] Lee B 2003 Review of the present status of optical fiber sensors *Opt. Fiber Technol.* **9** 57–79
[14] Deivasigamani A, Daliri A, Wang C H and John S 2013 A review of passive wireless sensors for structural health monitoring *Mod. Appl. Sci.* **7** 57–76
[15] Chawla V and Ha D S 2007 An overview of passive RFID *IEEE Commun. Mag.* **45** 11–7
[16] Weinstein R 2005 RFID: a technical overview and its application to the enterprise *IT Prof.* **7** 27–33
[17] Karmakar N C 2010 *Handbook of Smart Antennas for RFID Systems* (Hoboken, NJ: Wiley)

[18] Opasjumruskit K *et al* 2006 Self-powered wireless temperature sensors exploit RFID technology *IEEE Pervasive Comput.* **5** 54–61

[19] Bhattacharyya R, Floerkemeier C and Sarma S 2010 RFID tag antenna based temperature sensing *2010 IEEE Int. Conf. on RFID (IEEE RFID 2010)* pp 8–15

[20] Sample A P, Yeager D J, Powledge P S, Mamishev A V and Smith J R 2008 Design of an RFID-based battery-free programmable sensing platform *IEEE Trans. Instrum. Meas.* **57** 2608–15

[21] Kocer F and Flynn M P 2006 An RF-powered, wireless CMOS temperature sensor *IEEE Sens. J.* **6** 557–64

[22] Xu C, Gao P, Che W, Tan X, Yan N and Min H 2009 An ultra-low-power CMOS temperature sensor for RFID applications *J. Semicond.* **30** 045003

[23] Wang Y, Jia Y, Chen Q and Wang Y 2008 A passive wireless temperature sensor for harsh environment applications *Sensors* **8** 7982–95

[24] Yi X *et al* 2011 Passive wireless smart-skin sensor using RFID-based folded patch antennas *Int. J. Smart Nano Mater.* **2** 22–38

[25] Yi X, Cho C, Cooper J, Wang Y, Tentzeris M M and Leon R T 2013 Passive wireless antenna sensor for strain and crack sensing—electromagnetic modeling, simulation, and testing *Smart Mater. Struct.* **22** 085009

[26] Yi X, Wu T, Wang Y and Tentzeris M M 2015 Sensitivity modeling of an RFID-based strain-sensing antenna with dielectric constant change *IEEE Sens. J.* **15** 6147–55

[27] Yi X, Cho C, Cook B, Wang Y, Tentzeris M M and Leon R T 2013 Design and simulation of a slotted patch antenna sensor for wireless strain sensing *Proc. SPIE* **8694** 86941J

[28] Li D, Cho C and Wang Y 2017 Patch antenna sensor rosettes for surface strain measurement *Smart Infrastruct. Constr.* **170** 39–49

[29] Merilampi S, Björninen T, Ukkonen L, Ruuskanen P and Sydänheimo L 2011 Embedded wireless strain sensors based on printed RFID tag *Sens. Rev.* **31** 32–40

[30] Occhiuzzi C, Paggi C and Marrocco G 2011 Passive RFID strain-sensor based on meander-line antennas *IEEE Trans. Antennas Propag.* **59** 4836–40

[31] Preradovic S and Karmakar N 2010 Chipless RFID tag with integrated sensor *2010 IEEE Sensors* pp 1277–81

[32] Girbau D, Ramos Á, Lazaro A, Rima S and Villarino R 2012 Passive wireless temperature sensor based on time-coded UWB chipless RFID tags *IEEE Trans. Microw. Theory Tech.* **60** 3623–32

[33] Karmakar N C, Amin E M and Saha J K 2016 *Chipless RFID Sensors* (Hoboken, NJ: Wiley)

[34] Balanis C A 2005 *Antenna Theory Analysis and Design* 3rd edn (Hoboken, NJ: Wiley)

[35] Guo X *et al* 2017 Flexible and reversibly deformable radio-frequency antenna based on stretchable SWCNTs/PANI/Lycra conductive fabric *Smart Mater. Struct.* **26** 105036

[36] Guo X, Huang Y, Pan W, Kan W, Mao L and Zhang Y 2017 Flexible and deformable monopole antenna based on silver nanoparticles for wearable electronics *Nanosci. Nanotechnol. Lett.* **11** 1632–8

[37] Guo X, Huang Y, Die Z, Gao L and Liu C 2017 Flexible and wearable 2.45 GHz CPW-fed antenna using inkjet-printing of silver nanoparticles on pet substrate *Microw. Opt. Technol. Lett.* **59** 204–8

[38] Sanders J, Yao J and Huang H 2015 Microstrip patch antenna temperature sensor *IEEE Sens. J.* **15** 1

[39] Yao J, Mbanya Tchafa F, Jain A, Tjuatja S and Huang H 2016 Far-field interrogation of microstrip patch antenna for temperature sensing without electronics *IEEE Sens. J.* **16** 7053–60

[40] Mbanya Tchafa F, Yao J and Huang H 2016 Wireless interrogation of a high temperature antenna sensor *ASME Int. Mechanical Engineering Congress Exposition* vol 9V009T17A012

[41] Yan D *et al* 2017 AIN-based ceramic patch antenna-typewireless passive high-temperature sensor *Micromachines* **8** 301

[42] Cheng H, Ebadi S, Ren X and Gong X 2015 Wireless passive high-temperature sensor based on multifunctional reflective patch antenna up to 1050 degrees centigrade *Sensors Actuators* A **222** 204–11

[43] Tata U, Huang H, Carter R L and Chiao J C 2009 Exploiting a patch antenna for strain measurements *Meas. Sci. Technol.* **20** 015201

[44] Xu X and Huang H 2012 Battery-less wireless interrogation of microstrip patch antenna for strain sensing *Smart Mater. Struct.* **21** 125007

[45] Yi X, Cho C, Cook B, Wang Y, Tentzeris M M and Leon R T 2014 A slotted patch antenna for wireless strain sensing *Structures Congress 2014* pp 2734–43

[46] Qian Z, Tang Q, Li J, Zhao H and Zhang W 2012 Analysis and design of a strain sensor based on a microstrip patch antenna *2012 Int. Conf. Microwave Millimeter Wave Technology* vol 5, pp 1–3

[47] Wang W, Liu T, Ge H and Liu M 2015 Strain measurement based on microstrip patch antennas *2015 Annual Reliability and Maintainability Symp. (RAMS) (May 2015pp 1–6*

[48] Daliri A, Galehdar A, Rowe W S T, Ghorbani K and John S 2012 Utilising microstrip patch antenna strain sensors for structural health monitoring *J. Intell. Mater. Syst. Struct.* **23** 169–82

[49] Cho C, Yi X, Li D, Wang Y and Tentzeris M M 2016 Passive wireless frequency doubling antenna sensor for strain and crack sensing *IEEE Sens. J.* **16** 5725–33

[50] Evaluation S S 2018 A circular microstrip antenna sensor for direction sensitive strain evaluation *Sensors* **18** 310

[51] Daliri A, Galehdar A, John S, Wang C H, Rowe W S T and Ghorbani K 2012 Wireless strain measurement using circular microstrip patch antennas *Sensors Actuators* A **184** 86–92

[52] Maurya S, Yadava R L and Yadav R K 2013 Effect of temperature variation on microstrip patch antenna and temperature compensation technique *Int. J. Wirel. Commun. Mob. Comput.* **1** 35

[53] Yadav R K, Kishor J and Yadava R L 2013 Effects of temperature variations on microstrip antenna *Int. J. Netw. Commun.* **3** 21–4

[54] Yi X, Vyas R, Cho C, Fang C, Cooper J and Wang Y 2012 Thermal effects on a passive wireless antenna sensor for strain and crack sensing *Proc. SPIE* **8345** 83450F

[55] Carver K R and Mink J W 1981 Microstrip antenna technology *IEEE Trans. Antennas Propag.* **29** 2–24

[56] Rogers Corporation RT/duroid 5870/5880 high frequency laminates

[57] Yao J, Tjuatja S and Huang H 2015 Real-time vibratory strain sensing using passive wireless antenna sensor *IEEE Sens. J.* **15** 4338–45

[58] Davis J 1998 *Metals Handbook Desk Edition*

[59] Figliola R S and Beasley D E 2011 *Theory and Design for Mechanical Measurements* 5th edn (Hoboken, NJ: Wiley)